

## Core Formation, Coherence and Collapse: A New Core Evolution Paradigm Revealed by Machine Learning

HOPE HOW-HUAN CHEN,<sup>1</sup> STELLA S. R. OFFNER,<sup>1</sup> JAIME E. PINEDA,<sup>2</sup> ALYSSA A. GOODMAN,<sup>3</sup> ANDREAS BURKERT,<sup>4</sup>  
ADAM GINSBURG,<sup>5</sup> AND SPANDAN CHOUDHURY<sup>2</sup>

<sup>1</sup>*Department of Astronomy, The University of Texas, Austin, TX 78712, USA*

<sup>2</sup>*Max-Planck-Institut für extraterrestrische Physik, Giesenbachstrasse 1, D-85748 Garching, Germany*

<sup>3</sup>*Harvard-Smithsonian Center for Astrophysics, 60 Garden St., Cambridge, MA 02138, USA*

<sup>4</sup>*University Observatory Munich (USM), Scheinerstrasse 1, 81679 Munich, Germany*

<sup>5</sup>*Department of Astronomy, University of Florida, PO Box 112055, USA*

### ABSTRACT

We study the formation, evolution and collapse of dense cores by tracking density structures in a magnetohydrodynamic (MHD) simulation. We identify cores using the dendrogram algorithm and utilize machine learning techniques, including principal component analysis (PCA) and the  $k$ -means clustering algorithm to analyze the full density and velocity dispersion profiles of these cores. We find that there exists an evolutionary sequence consisting of three distinct phases: i) the formation of turbulent density structures (Phase I), ii) the dissipation of turbulence and the formation of coherent cores (Phase II), and iii) the transition to protostellar cores through gravitational collapse (Phase III). In dynamically evolving molecular clouds, the existence of these three phases corresponds to the coexistence of three populations of cores with distinct physical properties. The prestellar and protostellar cores frequently analyzed in previous studies of observations and simulations belong to the last phase in this evolutionary picture. We derive typical lifetimes of  $1.4 \pm 1.0 \times 10^5$  yr,  $3.3 \pm 1.4 \times 10^5$  yr and  $3.3 \pm 1.4 \times 10^5$  yr, respectively for Phase I, II and III. We find that cores can form from both converging flows and filament fragmentation and that cores may form both inside and outside the filaments. We then compare our results to previous observations of coherent cores and provide suggestions for future observations to study cores belonging to the three phases.

*Keywords:* Star Formation — Molecular Clouds — Magnetohydrodynamical Simulations — Interstellar Dynamics — Astrostatistics Techniques — Principal Component Analysis — Clustering

### 1. INTRODUCTION

Since the first identification of dense cores in molecular line observations made by Myers et al. (1983), astronomers have used the term “core” to describe the small ( $\sim 0.1$  pc; Jijina et al. 1999), roundish (aspect ratio  $\leq 2$ ; Myers et al. 1991) and quiescent (velocity dispersion nearly thermal; Fuller & Myers 1992) blobs of gas that are likely progenitors of low-mass stars. Later observations further characterized most star-forming cores as gravitationally bound, if not collapsing (Caselli et al. 2002; Enoch et al. 2008; Seo et al. 2015). On the other hand, Shu et al. (1987) formulated analytical star formation models and proposed an evolutionary sequence that describes the formation of protostars within cores through continuous accretion initiated by gravitational collapse and regulated by thermal pressure. Efforts using both observations and numerical simulations to understand the evolution of dense cores have since been largely focused on how dense cores evolve from the point of time when they become self-gravitating (“prestellar cores”) to when protostars form within them (“protostellar cores”; Li et al. 2004; Tafalla et al. 2004; McKee & Ostriker 2007; Offner et al. 2008; Lada et al. 2008; Kauffmann et al. 2008; Rosolowsky et al. 2008a; Dib et al. 2010; Chen & Ostriker 2018).

Barranco & Goodman (1998) used observations of NH<sub>3</sub> hyperfine line emission to show that the line widths in the interiors of some dense cores are roughly constant at a value slightly higher than a purely thermal line width. Goodman

et al. (1998) made observations of OH and C<sup>18</sup>O line emission of dense cores and proposed that a characteristic radius exists where the scaling law between the line width and the core size changes from a power law to a virtually constant relationship. Goodman et al. (1998) found this characteristic radius to be  $\sim 0.1$  pc and called the change in the line width–size relation the “transition to coherence.” A “coherent core,” defined by the transition to coherence, is hypothesized to provide the ideal low-turbulence environment for further star formation through gravitational collapse (Goodman et al. 1998; Caselli et al. 2002). At around the same time, by measuring the near-infrared extinction, Alves et al. (2001) found that the internal density structures of the dark cloud Barnard 68 are well described by a pressure-confined, self-gravitating isothermal sphere that is critically stable according to the Bonnor-Ebert criteria (Ebert 1955; Bonnor 1956). Later observations of C<sup>18</sup>O molecular line emission confirmed that Barnard 68 is a thermally supported dense core (although a later study found evidence that Barnard 68 is possibly merging with a smaller structure, which would lead to destabilization and collapse; Lada et al. 2003; Burkert & Alves 2009). Both the observation of coherent cores and the identification of a thermally supported dense core resembling a critical Bonnor-Ebert sphere provide important hints about the initial condition of dense cores before the formation of protostars within them.

Recent observational works have revealed that coherent cores are common in nearby molecular clouds. Pineda et al. (2010) made the first direct observation of a coherent core in the B5 region in Perseus. Pineda et al. (2010) observed NH<sub>3</sub> hyperfine line emission using the Green Bank Telescope (GBT) and resolved the transition to coherence across the boundary of the core. Using Very Large Array (VLA) observations of the interior of the coherent core in B5, Pineda et al. (2015) found substructures within the B5 coherent core that will likely form protostars in a freefall time of  $\sim 40,000$  yr. Chen et al. (2019a) identified a population of at least 18 coherent structures<sup>1</sup> in Ophiuchus and Taurus using data from the GBT Ammonia Survey (GAS; Friesen et al. 2017). These include “droplets,” a population of coherent cores that are not bound by self-gravity but are predominantly confined by the pressure provided by the turbulent motions of the ambient gas (Chen et al. 2019a). The non-self-gravitating droplets have density structures shallower than a critical Bonnor-Ebert sphere (Chen et al. 2019a) and sometimes show signs of internal velocity gradients that are likely the result of a combination of turbulent and rotational motions (Chen et al. 2019b). It was conjectured that these coherent structures, not bound by self-gravity, are either i) at an early stage of core formation, ii) an extension of the more massive coherent core population, or iii) transient. Together, Pineda et al. (2010) and Chen et al. (2019a) revealed an entire population of coherent cores, ranging from self-gravitating and sometimes star-forming ones, including the B5 coherent core, to non-self-gravitating and predominantly pressure-confined droplets. If coherent cores do indeed provide the necessary low-turbulence environment for star formation as hypothesized by Goodman et al. (1998), then an important question concerns whether there is an evolutionary relation between different “flavors” of coherent cores and between coherent cores and the better known pre-/protostellar cores. Unfortunately, no coherent cores defined by a transition to coherence have been identified in simulations to date, although cores with subsonic velocity dispersions have been identified in simulations (e.g., Klessen et al. 2005).

In this work, we develop a method to identify, track and characterize the evolution of dynamic gas structures in simulations, which may be applied to other numerical models of star formation. We aim to provide a complete picture of core formation and evolution that links turbulent molecular clouds to star-forming cores. In particular, we aim to answer the following questions: i) how do cores form in a turbulent environment, ii) what role do coherent cores play in the evolution of cores, and iii) is there an evolutionary connection between coherent cores and pre-/protostellar cores? To answer these questions, we carry out a comprehensive analysis of density structures in a magnetohydrodynamic (MHD) simulation of a turbulent molecular cloud. We examine these structures as they evolve and move across the simulation without any prior assumptions regarding their internal structures. We achieve this by utilizing unsupervised machine learning techniques including principal component analysis (PCA) and a *k-means* clustering algorithm. We then compare our results to the known coherent cores identified by Chen et al. (2019a), which provide important constraints on the full population of coherent cores.

In §2, we first describe the MHD simulation, as well as the set of observations that we compare to. We then introduce our method to identify density structures in §3.1, the principal component analysis in §3.2, the clustering algorithm used to analyze the PCA results in §3.3 and the way we track structures across different time steps of the MHD simulation in §3.4. We examine the core evolution and summarize the results in §4. We then discuss the implication

<sup>1</sup> In this work, “coherent cores” and “coherent structures” are used interchangeably to refer to dense cores defined by a transition to coherence. The non-self-gravitating and pressure confined population of “droplets” identified by Chen et al. (2019a) is a subset of coherent cores by this definition. This slightly differs from the convention adopted by Chen et al. (2019a), where the term “coherent cores” specifically means self-gravitating coherent cores. See §3 in Chen et al. (2019a).

of the existence of an evolutionary sequence in §5.1 and provide a comparison with existing observations as well as a discussion of observational limitations in §5.2. We summarize our work in §6.

## 2. DATA

### 2.1. MHD Simulation

We analyze the magnetohydrodynamic (MHD) simulation of a turbulent star-forming cloud from Smullen et al. (2020). The simulation models a box of 5 pc on a side with periodic boundary conditions. We focus on the data in the basegrid and first adaptive mesh refinement (AMR) level, which corresponds to a voxel size of  $\sim 0.010$  pc and is consistent with a Nyquist sampling of the beam size of observations used by Chen et al. (2019a). The initial conditions of this simulation are identical to those of run W2T2 in Offner & Arce (2015), where these conditions are chosen to model a typical nearby molecular cloud like the Perseus molecular cloud. The simulation is run using the ORION2 code and includes ideal MHD, self-gravity and Lagrangian accreting sink particles (Krumholz et al. 2004, 2007; Li et al. 2012). The mean gas density of the simulation is  $\rho_0 = 2 \times 10^{-21}$  g cm $^{-3}$ , or  $\sim 430$  cm $^{-3}$  in number density assuming a mean molecular weight per H $_2$  molecule of 2.8 a.m.u. (Kauffmann et al. 2008). The simulation begins with a uniform density, a uniform temperature of 10 K and a uniform magnetic field in the  $z$ -direction,  $B_z = 13.5$   $\mu$ G. The gas is then perturbed for two Mach crossing times by a random velocity distribution that corresponds to a flat distribution in Fourier space with wave numbers  $k = 1 - 2$ . At the end of the driving phase, the gas reaches a turbulent steady state with a turbulent power spectrum  $P(k) \propto k^{-2}$  and plasma parameter (ratio of thermal pressure to magnetic pressure),  $\beta = 8\pi\rho_0 c_s^2 / B_z^2 = 0.02$ , where  $c_s$  is the sonic speed (Offner & Arce 2015). See Smullen et al. (2020) for details.

### 2.2. Source Catalogs

We compare the cores identified in the MHD simulation to the cores observed by Chen et al. (2019a). Chen et al. (2019a) identified a population of 18 coherent structures in two star-forming regions in nearby molecular clouds, L1688 in Ophiuchus and B18 in Taurus, using observations of NH $_3$  emission from the GBT Ammonia Survey (Friesen et al. 2017) and column density maps derived from Herschel observations of dust emission (André et al. 2010). These cores are identified by a transition to coherence at their boundaries and a subsonic turbulent velocity dispersion in their interiors. The typical mass of the cores is  $0.4^{+0.4}_{-0.3}$  M $_{\odot}$ , and the typical radius is  $0.04 \pm 0.01$  pc. Chen et al. (2019a) found that the cores have a typical total velocity dispersion,  $\sigma_{\text{tot}} = \sqrt{\sigma_{\text{turb}}^2 + \sigma_{\text{therm}}^2} = 0.22 \pm 0.02$  km s $^{-1}$ , where  $\sigma_{\text{turb}}$  is the turbulent velocity dispersion and  $\sigma_{\text{therm}}$  is the thermal velocity dispersion. These cores have density profiles shallower than a critical Bonnor-Ebert sphere, and they are not bound by self-gravity but are instead bound by pressure provided by the ambient gas motion, i.e., the turbulent pressure.

## 3. ANALYSIS

To carry out a comprehensive analysis of independent density structures in the MHD simulation, we first identify these structures using the dendrogram algorithm<sup>2</sup>. We next classify the structures by performing a PCA and  $k$ -means analysis on their density and velocity dispersion profiles. Finally, we track each independent structure in the dendrogram as it evolves and moves across both the simulation and the PCA space. Fig. 1 is a schematic summary of our analysis procedure.

### 3.1. Core Identification

We identify cores in each snapshot of the MHD simulation described in §2.1 using the dendrogram algorithm (using the *astrodendro* package, which implements a dendrogram-based core extraction algorithm; Rosolowsky et al. 2008b; Goodman et al. 2009b). Dendrogram-based algorithms efficiently identify density structures in star-forming regions in both simulations (e.g., Burkhardt et al. 2013; Koch et al. 2017) and observations (e.g., Goodman et al. 2009b; Seo et al. 2015). For each snapshot, we apply the dendrogram on the density distribution in the 3D space. We construct the dendrogram to find structures with densities above  $10^4$  cm $^{-3}$ . To guarantee enough sampling points for the analysis of density and velocity distributions, a structure must have a volume of at least 100 voxels ( $\sim 0.028$  pc in the linear size) to be included in the dendrogram. To avoid the inclusion of insignificant local density fluctuations, a structure must also have a difference of  $10^4$  cm $^{-3}$  in density between its peak and the node where it merges onto the tree<sup>3</sup>. We

<sup>2</sup> We use *astrodendro*, a *Python* package to compute dendrograms of astronomical data (<http://dendrograms.org>).

<sup>3</sup> These setup parameters translate to *min\_value* of  $10^4$  cm $^{-3}$ , *min\_delta* of  $10^4$  cm $^{-3}$  and *min\_npix* of 100 in *astrodendro*. A “tree” is a full dendrogram representation of hierarchical structures.

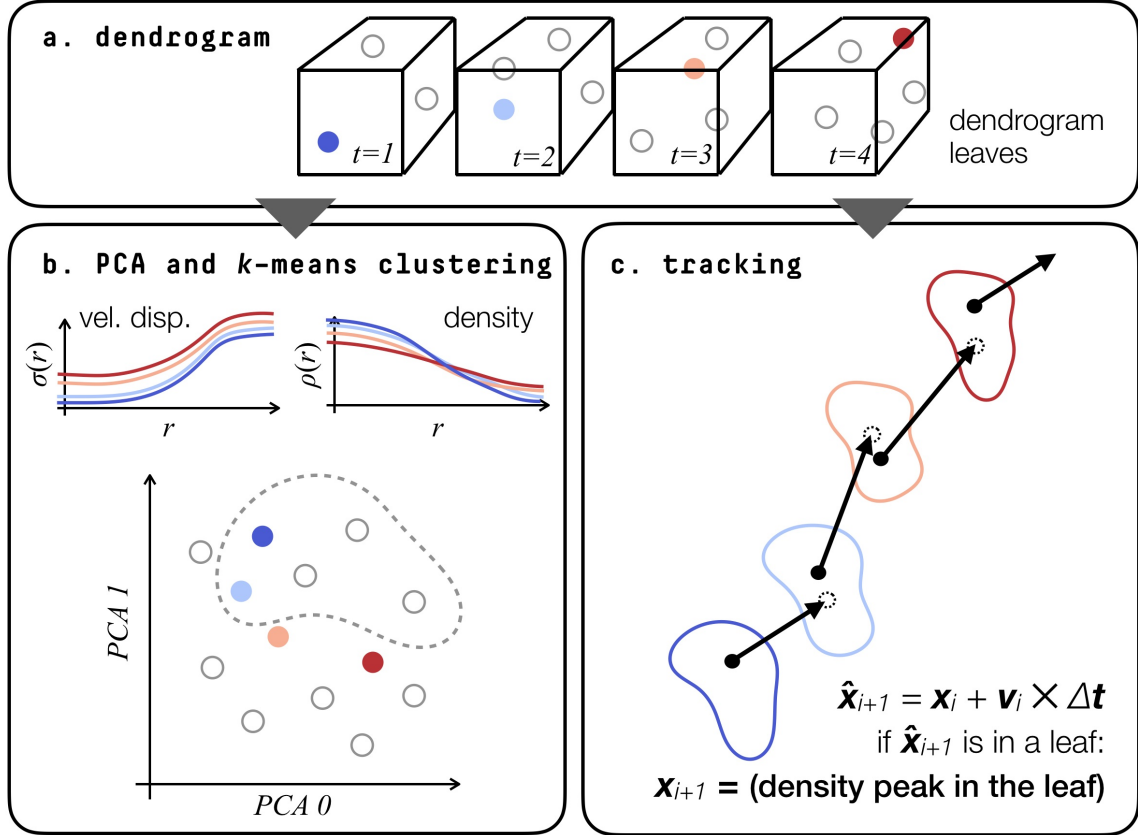


**Figure 1.** Schematic summary of the analyses carried out in this work. (a) Density structure identification using dendrogram. (b) PCA analysis and  $k$ -means clustering analysis on the density and velocity dispersion profiles. (c) Tracking each density structure as it moves and evolves across the simulation. Note that the PCA analysis and tracking are done independently from each other.

identify a total of 2,422 structures over a time span of  $6.0 \times 10^5$  years, with a nominal time resolution of  $2.1 \times 10^4$  years. Note that we use the dendrogram only to identify independent density structures and locate their peaks. We do not limit our following analysis of the density distribution to only the density range above  $10^4 \text{ cm}^{-3}$  (see §3.4 for details), and we only use the dendrogram boundary to avoid confusion with a neighboring core. See Fig. 2 for an example of the independent structures identified using the dendrogram algorithm.

### 3.2. Principal Component Analysis of Density and Velocity Dispersion Profiles

To study the properties of the structures identified in §3.1, we carry out a PCA analysis on the radial profiles of the density and velocity dispersion. We take the following steps to derive the radial profiles. First, we draw a series of constant density isosurfaces, each at a number density  $n_i$ . We use 50 density values uniformly spaced on a logarithmic scale between  $n = 10^{2.5} \text{ cm}^{-3}$  and  $10^{5.5} \text{ cm}^{-3}$ . As Fig. 3 shows, these densities well sample the underlying probability density function (PDF) of density. Each isosurface is then converted to an equivalent radius by finding the radius that would construct a sphere that has the same volume as the volume enclosed by the isosurface, i.e.,  $V_{\text{iso}} = 4\pi R_{\text{eq}}^3/3$ . The radial density profile,  $n(r)$ , is then constructed from the series of densities,  $n_i$ , that define the isosurfaces and the corresponding equivalent radii,  $R_{\text{eq},i}$ . For the velocity dispersion profile, we calculate the velocity dispersion of material enclosed within each isosurface,  $\sigma_i$ , and similarly construct the profile of velocity dispersion,  $\sigma(r)$ , from  $\sigma_i$  and  $R_{\text{eq},i}$ . To avoid confusion with another core, we stop the construction of profiles when the volume enclosed by the isosurface overlaps with the dendrogram boundary of another core. This occurs mostly when the core has a *sibling*, i.e., a nearby leaf that has the same density minimum and shares the same *parent* branch in the dendrogram. For a core that does not have a sibling (the “trunk-leaves”—independent structures at the bottom level; Rosolowsky et al.

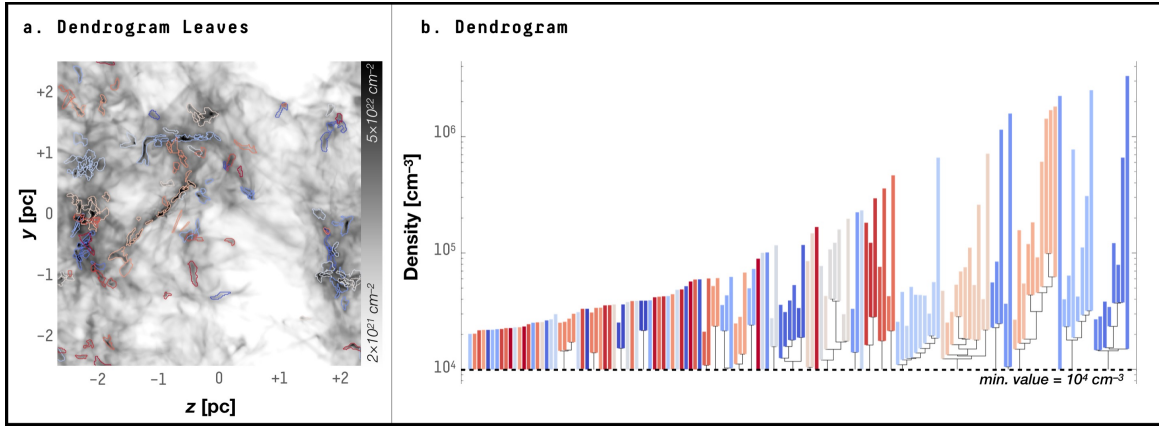


**Figure 2.** Cores identified as dendrogram leaves. (a) Dendrogram structures plotted on top of the density field integrated over the x-axis. The contours are color coded according to the ID number the *astro dendro* package assigns, and each corresponds to the structure in the dendrogram with the same color. (b) Dendrogram with the leaves color coded by the ID number the *astro dendro* package assigns. This snapshot is at  $t = 5 \times 10^5$  yr. Note that since neighboring structures in the dendrogram are usually assigned consecutive ID numbers, structures that share the same branch may have a difference in color too subtle to be recognized by eye.

2008b), the profile is derived for radii beyond the boundary defined by the dendrogram. This method does not involve spherical averaging and can produce radial profiles for structures with different shapes in a reliable and consistent way.

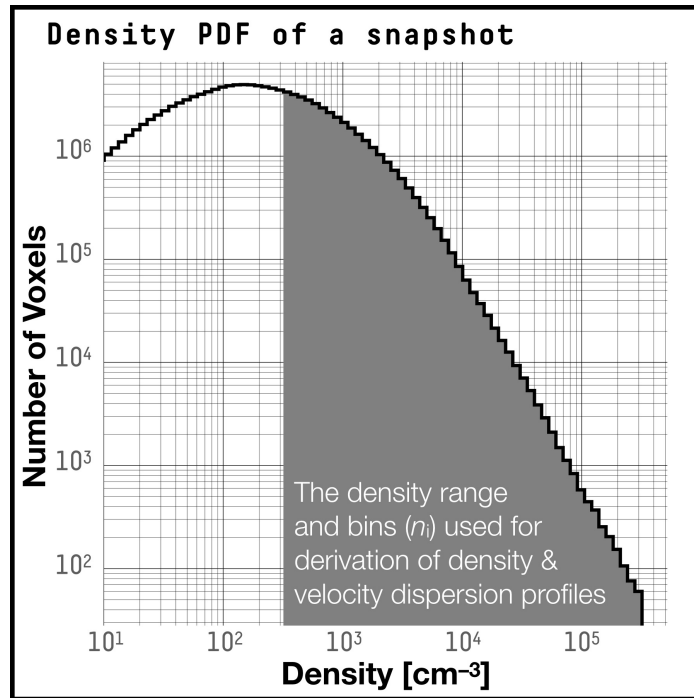


**Figure 3.** Probability density function (PDF) of density of a snapshot taken at  $t = 5 \times 10^5$  yr (solid black line). The shaded area and bins correspond to the range of density and the series of  $n_i$  used for deriving the density and velocity dispersion profiles (see §3.2).

We apply PCA on the radial profiles of the density and velocity dispersion. PCA is a statistical procedure that applies an orthogonal transformation to a set of data and converts them into a set of linearly uncorrelated components called principal components. PCA is defined such that the first principal components account for the largest possible variations in the set of observations, here the radial density and velocity dispersion profiles. PCA is suitable for our task

to explore the evolution of density structures in two aspects. First, it does not require any *a priori* assumption about the shapes of the radial density and velocity dispersion profiles. Second, it is effective in reducing the high dimensional information in the radial density and velocity dispersion profiles. We use the first six principal components from the PCA analysis in the following study, which account for 67.5%, 23.2%, 3.7%, 3.3%, 1.0%, and 0.5% of the variance in the input density and velocity dispersion profiles, respectively. In total, the first six principal components account for 99.2% of the variance in the input radial profiles. The first two components of the PCA analysis are shown in Fig. 4. For reference, we also explored the t-distributed stochastic neighbor embedding (t-SNE) as a means of information density reduction. See discussion in Appendix A.

### 3.3. Clustering of the PCA Components

To analyze the distribution of the PCA components, we employ a  $k$ -means clustering algorithm. For a designated number of groups expected in the final clustering,  $k$ , the  $k$ -means algorithm starts with  $k$  randomly selected data points as the initial *means*. Here, the relevant parameter space for clustering is described by the values of the first 6 PCA components (see §3.2). The  $k$ -means algorithm then partitions the data distribution into  $k$  groups by assigning each data point to the closest of the  $k$  means using the squared Euclidean distance. The algorithm then calculates a new set of  $k$  means based on the data points in each of the  $k$  groups and uses the new  $k$  means to partition the data in the next iteration. Eventually the partitioning converges to a clustering result that minimizes the variance within each cluster and maximizes the sum of variances between data points in different clusters.

To find the optimal number of clusters, we experimented with  $k = 2, 3, 4$  and  $5$  and observed the physical properties of structures within each cluster. We find that when  $k = 3$ , the structures are clustered into three groups with characteristically distinct properties in velocity dispersion and density distribution. Larger  $k$  returns clusters that appear to partition the distribution into groups with apparently similar velocity dispersions, while  $k = 2$  is only sensitive to the density distribution but not the velocity dispersion. For the purpose of analyzing the general evolutionary trends in density and velocity dispersion distributions, we focus on the clustering derived with  $k = 3$  and leave the analysis of potentially latent subgroups to the future. We do note that one limitation of the  $k$ -means approach is that the result depends on this initial choice of cluster number. We also note that the PCA distribution appears to be continuous, and it is not immediately obvious by eyes that there are three distinct groups. We will discuss the smoothness of the PCA distribution below in §5.1. Fig. 5 shows the clustering result.

### 3.4. Tracking

Independent from the PCA and clustering analyses, we devise a tracking procedure by first identifying the density peaks within independent structures, *leaves*, in the dendrogram of each snapshot. The tracking procedure then uses the velocity at the position of the density peak to predict where the density peak is expected to be in the previous and following snapshots. If the expected position falls within the boundary of a dendrogram leaf, the tracking procedure “links” the original structure with the leaf in the previous or following snapshot. This tracking procedure is similar to but less detailed than the one deployed and analyzed by Smullen et al. (2020), in which the overlap in various physical quantities and statistical measurements are examined when dendrogram structures in different snapshots are compared. Our tracking procedure then repeats the process by going through the total of 2,422 independent structures of the dendrograms derived for the snapshots used in this study. We find that 2,083 out of 2,422 structures ( $\sim 86\%$ ) are connected to one of a total of 241 evolutionary tracks and that the average time span of a track is  $1.3 \times 10^5$  years. As Smullen et al. (2020) have pointed out, the robustness of the identification using the dendrogram algorithm is subject to uncertainties due to the stochastic fluctuation in the density distribution over time, even when the dendrograms are derived using the same set of input parameters. We try to avoid the issue of density fluctuations affecting the robustness of dendrogram tracking by excluding structures that are not connected to any of the tracks. This is equivalent to removing structures that are captured by a dendrogram only in a certain snapshot but not the preceding nor the subsequent ones (separated by  $\Delta t \sim 2.1 \times 10^4$  yr; see §3.1). 24 out of the total of 241 tracks ( $\sim 10\%$ ) are each connected to at least one structure with a sink particle of a mass  $\geq 0.1 M_{\odot}$ . We use the tracking result in combination with the PCA and clustering analyses to probe the movement of structures in the PCA space as the structures evolve. See Fig. 6.

## 4. RESULTS

### 4.1. Core Classes and Evolution

The distribution of the first two PCA components is shown in Fig. 4. Comparing the distribution of the first two PCA components with the size of the coherent region and the index of a power-law fit to the density profile shows that cores with distinct density and velocity structures occupy different corners of the PCA space. Cores with extended coherent regions, defined by a subsonic turbulent velocity dispersion, generally have smaller first and second PCA components (Fig. 4a). Meanwhile, cores with steeper density profiles tend to have larger first PCA components (Fig. 4b). We also notice that cores with “young stellar objects (YSOs)” (sinks with masses  $\geq 0.1 M_{\odot}$ ) within them are clustered toward the corner of the PCA space with larger first PCA components and smaller second PCA components.

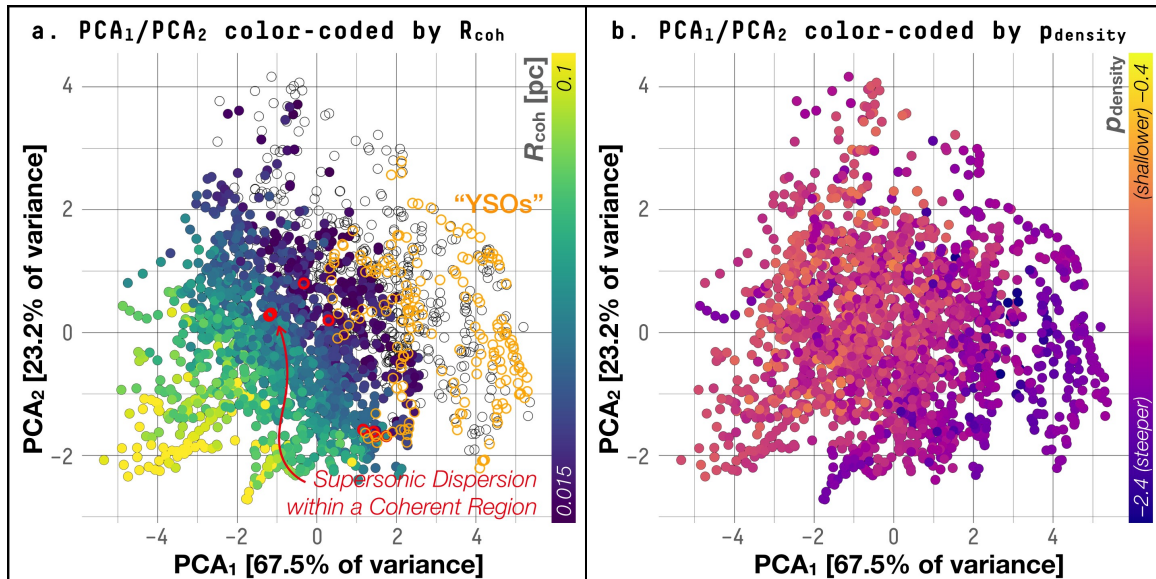


**Figure 4.** (a) Distribution of the first and second PCA components of all 2,083 independent structures, with the data points color coded by the size of the coherent region defined as the region within which the turbulence is subsonic. Each empty circle corresponds to a structure without a coherent region. Each data point with a yellow edge corresponds to a structure that has at least one sink particle with a mass  $\geq 0.1 M_{\odot}$  within its boundary, and each data point with a red edge corresponds to a structure where we find supersonic turbulent motions within (and usually near the center of) a coherent region. (b) Same as (a), but the data points are color coded by the index of the power law fitted to the radial density profile of each structure.

The clustering derived from the  $k$ -means analysis shows that the distribution of the PCA components can be partitioned into three groups (Fig. 5). Comparing the result from the  $k$ -means analysis to the physical properties shown in Fig. 4, we see that the three groups include populations of cores with different physical properties: i) the first group includes cores with larger velocity dispersions and shallower density profiles, ii) the second group includes cores that have subsonic turbulent velocity dispersions, and iii) the third group includes cores that have larger velocity dispersions and steep density profiles, within many of which YSOs have formed. These physical properties suggest that cores in the second group resemble observed coherent cores, while cores in the third group resemble star-forming cores including both prestellar and protostellar cores.

When we overlay the result from tracking the cores across different time steps, we find that the three groups are likely connected on an evolutionary track and represent three different evolutionary phases (Fig. 6a). Based on the tracking result, we refer to the three groups as Phase I, Phase II and Phase III. In this evolutionary picture, Phase I, II and III are closely related to i) the formation of turbulent over-densities, ii) the dissipation of turbulence and the formation of coherent regions, and iii) the onset of gravitational infall, which leads to star formation. This can be demonstrated by examining the difference in the core density and velocity dispersion profiles between phases.

As described in §3.2, the input to the PCA includes radial profiles of both the density and velocity dispersion of the cores. Fig. 7 and Fig. 8 show these density and velocity dispersion profiles in groups identified by the  $k$ -means analysis. We notice that the velocity dispersion profiles of the Phase II cores resemble that of a coherent core, with subsonic and nearly uniform velocity dispersion distribution near the center. Meanwhile, the cores in Phase I have supersonic velocity dispersions. In addition, the density profiles of the Phase I and Phase II cores are similar. This is

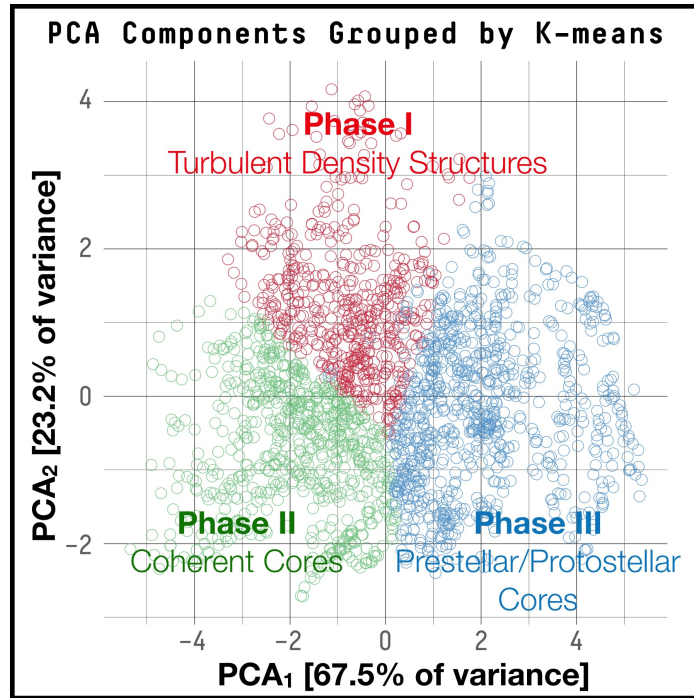


**Figure 5.** Distribution of the first two PCA components of all 2,083 independent structures, color coded by the result of a  $k$ -means clustering analysis on the PCA distribution. The red, green and blue circles mark the cores in Phase I, Phase II and Phase III, respectively.

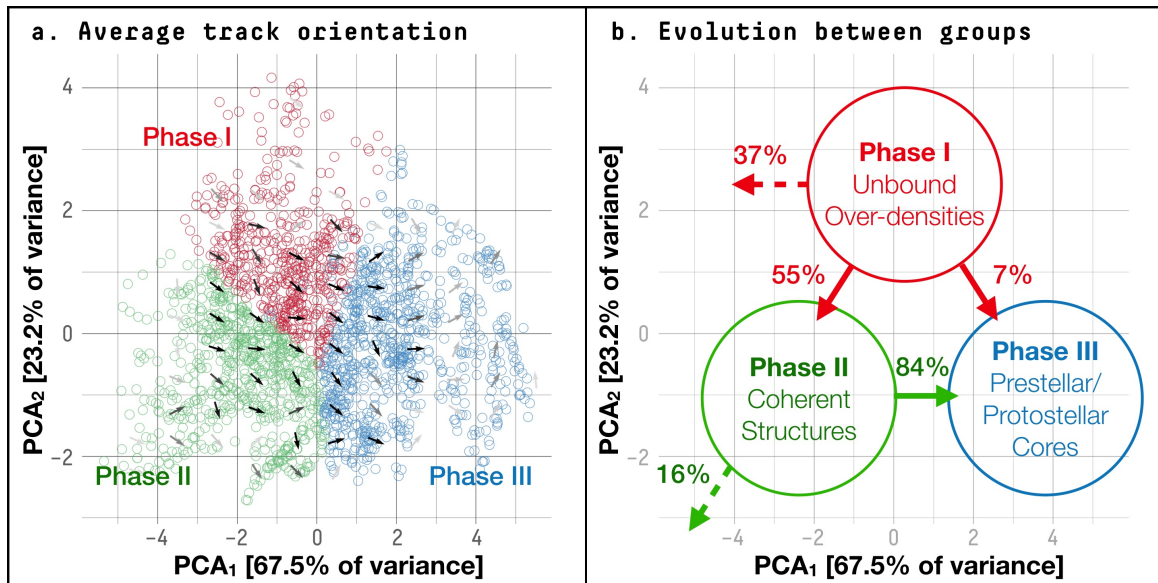


**Figure 6.** (a) Mean direction of evolutionary tracks overlaid on the distribution of PCA components. As in Fig. 5, the red, green and blue correspond to Phase I, II and III. The transparency of the arrows is proportional to the uncertainty estimated based on the number of tracks in each bin. (b) Ratios of structures from each phase that evolve into other phases (solid arrows) or disperse (dashed arrows).

consistent with a picture where the core dissipates its turbulence when evolving from Phase I to Phase II. This process corresponds to the formation of coherent cores.

On the other hand, the density profile of a core becomes noticeably steeper with a higher central density when the core evolves from Phase II to Phase III (Fig. 7). Meanwhile, the velocity dispersion of the core becomes supersonic again

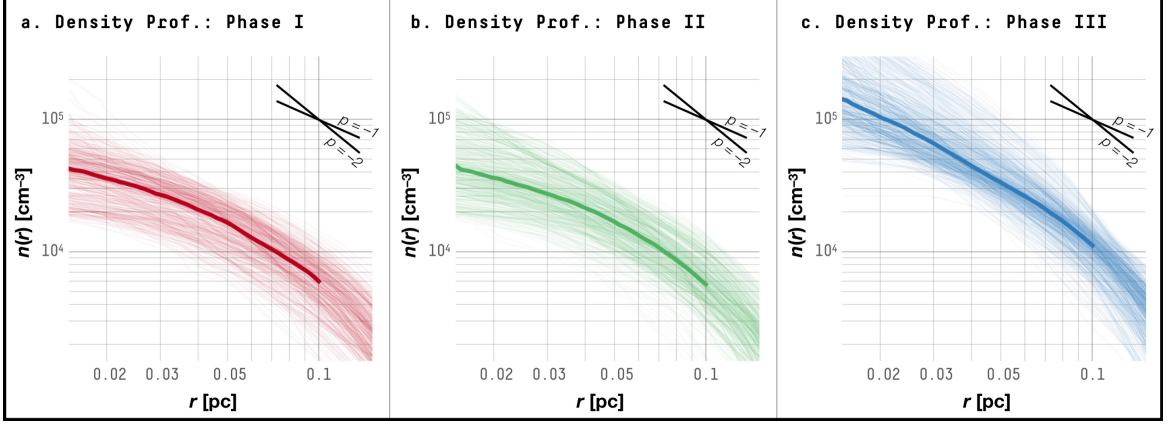


**Figure 7.** Radial profiles of density of cores in (a) Phase I, (b) Phase II and (c) Phase III. The thick line in each panel represents the median profile. For reference, the straight lines in the top-right corner of each panel show segments of two power-law functions with indices of  $-1$  and  $-2$ .

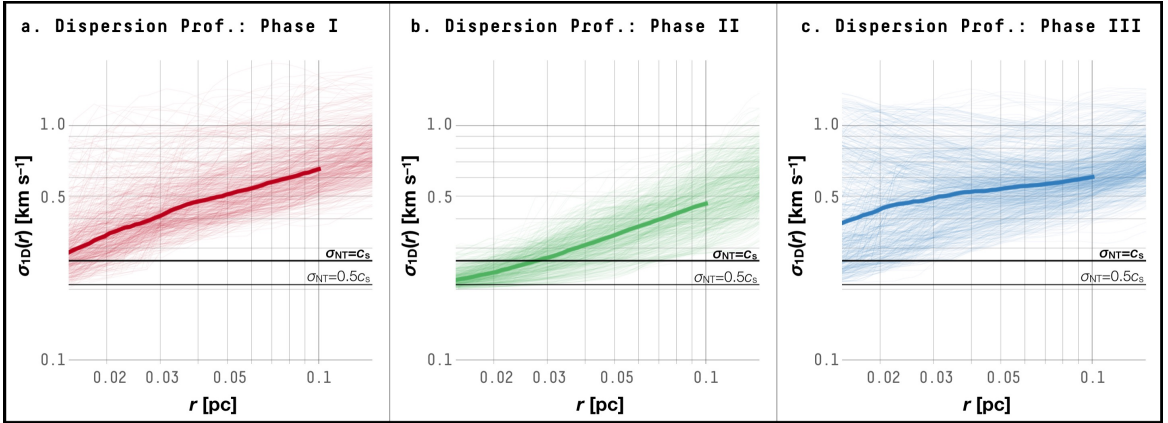


**Figure 8.** Radial profiles of velocity dispersion of structures in (a) Phase I, (b) Phase II and (c) Phase III. The thick line in each panel represents the median profile, and the horizontal black lines denote the velocity dispersion values when the turbulent velocity dispersion is equal to the sonic speed (thicker line) and half the sonic speed (thinner line) at 10 K.

with indications of enhanced velocity dispersion near the center (Fig. 8). This process is consistent with gravitational infall taking over the internal kinematics of the core. In summary, after the formation of a turbulent core (Phase I), it likely dissipates turbulence first (Phase II) and undergoes active gravitational infall only after a coherent region forms in the interior (Phase III).

#### 4.2. Survival Rates & Lifetimes

In §4.1, we show that there exists an evolutionary track connecting three populations of cores with different physical properties. A closer examination of the survival rates, defined as the fraction of cores evolving from one phase to the next, reveals that the evolutionary track is not monotonic. 55% of the Phase I cores evolve to become Phase II cores, while 7% of the cores in Phase I evolve to become Phase III cores (Fig. 6b). The rest 37% of the Phase I cores disperse and return the material to the environment at a later time. On the other hand, 84% of the Phase II cores evolve to become Phase III cores, and the rest (16%) disperses at a later time. This shows that core evolution is dynamic, and a core at a certain time along this evolutionary track can disperse later, with the survival rate generally increasing over time.

Combining the results from the tracking of the cores and the PCA analysis, we derive the time it takes a core to move one unit length in the PCA space as a function of location in the PCA space,  $\Delta t/\Delta s$  (Fig. 9). The timescale of each phase can then be estimated by integrating  $\Delta t/\Delta s$  along a path across the extent of each phase in the PCA space,  $t = \int (\Delta t/\Delta s) ds$ . Using this method, we estimate lifetimes of  $1.4 \pm 1.0 \times 10^5$  yr,  $3.3 \pm 1.4 \times 10^5$  yr and  $3.3 \pm 1.4 \times 10^5$  yr

for Phase I, II and III. We note that the uncertainty is mainly due to the fact that not all structures follow the same path, which would be represented by a single curve in the PCA space, as they evolve and move in the PCA space (see Fig. 6). The spread is likely explained by variation in the initial physical properties of the Phase I cores and/or variation in the physical conditions of the environment.

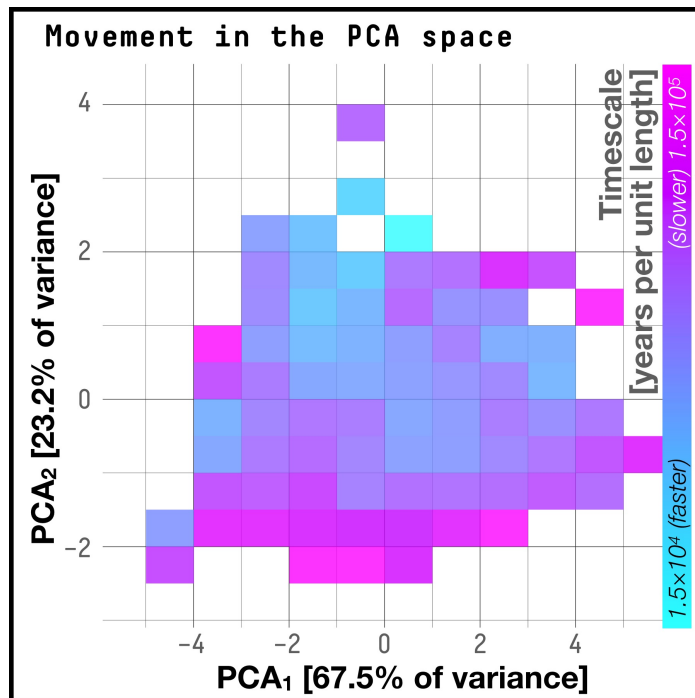


**Figure 9.** Average time it takes a structure to move one unit length in the PCA space, as a function of the location in the PCA space. The typical uncertainty in each bin is  $3 \times 10^4$  years per unit length in the PCA space.

#### 4.3. Core Properties

It is possible to derive a mass, a size and a density-weighted median velocity dispersion for each structure analyzed above. However, before going into any detailed analysis, we note that there is substantial uncertainty in the definition of the core. As Smullen et al. (2020) pointed out, there is no time-stable density contour that well defines a core, and the physical properties, including the mass, the size and the velocity dispersion, derived based on a density contour can vary by 20% to 50%. Using different definitions for the boundary, e.g., a constant density or a constant velocity dispersion, can significantly affect the numbers derived for the structure (see also Rosolowsky et al. 2008b). In this section we present an analysis of the physical properties derived using the boundary defined by the dendrogram algorithm, which finds the largest extent of a structure in the 3D space before it joins a neighboring structure in terms of their density distributions (see §3.1). See Smullen et al. (2020) for discussions on the observational effects on core property measurements.

Fig. 10a shows the mass as a function of size for the cores in each of the three phases. It appears that the three phases generally fall along a tight power-law relation. A power-law fit to the mass-size distribution of structures in all three phases gives a power-law index of  $\sim 2.5$ . Phase III cores appear to have slightly higher masses than those expected from this power-law relation. Note that the cores in the three phases have fairly different density distributions (see Fig. 7), and the fitted power-law relation should not be translated into one simple density profile. Fig. 10b shows the velocity dispersion as a function of size for the structures in each of the three phases. As expected from the velocity dispersion profiles examined in §4.1, Phase I and Phase III structures generally have larger velocity dispersions than Phase II structures.

Using the mass, the size and the velocity dispersion derived above (Fig. 10), we compare the kinetic energy to the gravitational potential energy in Fig. 11. Such a comparison, conventionally known as a *virial analysis*, provides a first-order estimate of the gravitational boundedness of a structure. A virial analysis may sometimes include other

**Table 1.** Physical Properties of Cores in Each Phase

	$M^a$	$R^b$	$\sigma_{\text{tot}}^c$	$\Omega_K^d$	$ \Omega_G ^e$	$\Omega_K/ \Omega_G ^f$	$p^g$	$\langle v \rangle^h$
	$M_\odot$	pc	$\text{km s}^{-1}$	erg	erg			$\text{km s}^{-1}$
Phase I	$1.73^{+1.66}_{-1.14}$	$0.07^{+0.02}_{-0.02}$	$0.33^{+0.12}_{-0.06}$	$6.4^{+8.1}_{-4.6} \times 10^{42}$	$2.2^{+4.5}_{-1.9} \times 10^{42}$	$2.8^{+4.0}_{-1.3}$	$-1.0^{+0.3}_{-0.2}$	$1.1 \pm 0.6$
Phase II	$1.86^{+2.49}_{-1.10}$	$0.07^{+0.02}_{-0.02}$	$0.23^{+0.05}_{-0.06}$	$2.9^{+5.5}_{-2.1} \times 10^{42}$	$2.4^{+7.8}_{-1.9} \times 10^{42}$	$1.1^{+1.0}_{-0.4}$	$-1.0^{+0.2}_{-0.2}$	$0.7 \pm 0.6$
Phase III	$7.14^{+3.78}_{-2.57}$	$0.10^{+0.01}_{-0.02}$	$0.35^{+0.10}_{-0.05}$	$2.8^{+2.5}_{-1.4} \times 10^{43}$	$2.5^{+2.7}_{-1.3} \times 10^{43}$	$1.1^{+0.6}_{-0.4}$	$-1.4^{+0.3}_{-0.3}$	$1.0 \pm 0.7$

<sup>a</sup>Mass. This and other physical properties are measured using the dendrogram leaf boundary to define a core.

<sup>b</sup>Radius.

<sup>c</sup>Total velocity dispersion.

<sup>d</sup>Kinetic energy.

<sup>e</sup>The absolute value of the gravitational potential energy.

<sup>f</sup>The ratio between the kinetic energy and the absolute value of the gravitational potential energy. Note that by definition, the conventional virial parameter is two times this ratio.

<sup>g</sup>The index of a simple power law,  $n = n_0(r/r_0)^p$ , fitted to the density profile of each core.

<sup>h</sup>The median bulk velocity magnitude of cores in each phase, with respect to the cloud.

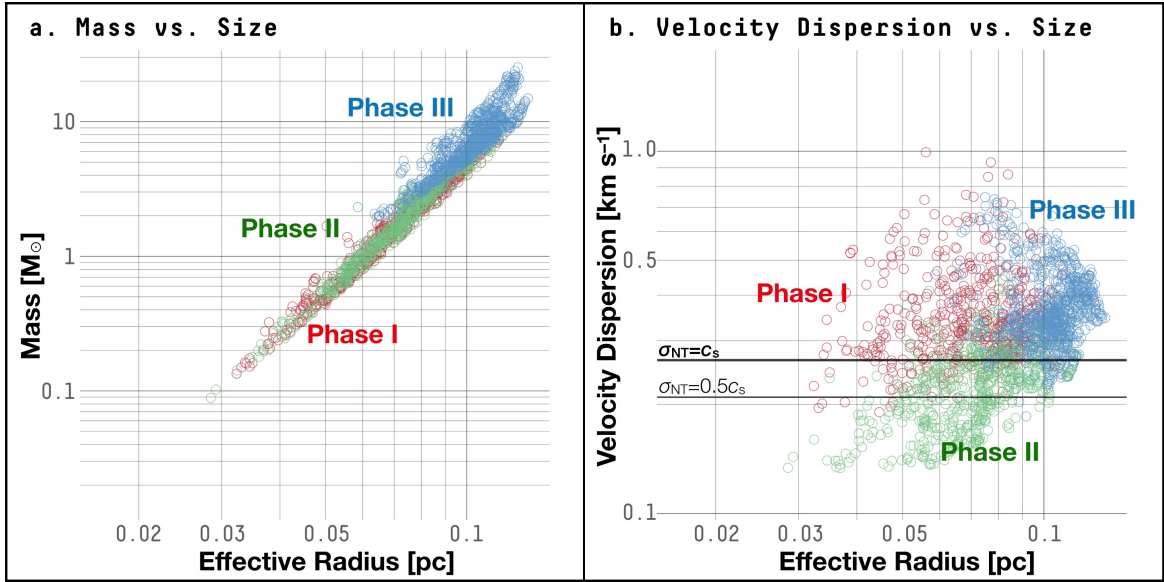


**Figure 10.** (a) Mass-size distribution of structures in Phase I (red circles), Phase II (green circles) and Phase III (blue circles). (b) Velocity dispersion-size distribution of structures in Phase I (red circles), Phase II (green circles) and Phase III (blue circles). The horizontal black lines denotes the velocity dispersion values when the non-thermal velocity dispersion is equal to the sonic speed (thicker line) and half the sonic speed (thinner line) at 10 K.

terms such as the magnetic energy and the surface pressure term (see Ward-Thompson et al. 2006; Pattle et al. 2015; Chen et al. 2019a). We find that Phase I cores are less bound by self-gravity than the cores in the other two phases. We also find that Phase III structures are more gravitationally bound, consistent with the star-forming activities found within many of them. Overall, the cores evolve toward virial equilibrium first (from Phase I to Phase II) and then follow along the line of virial equilibrium, while becoming more gravitationally bound (from Phase II to Phase III). The spread can be explained by the variation in the initial physical properties of the Phase I cores.

We also derive the bulk velocities of the cores in each phase. We find that the Phase I, Phase II and Phase III cores are moving with respect to the cloud at typical velocities of  $0.7 \pm 0.5 \text{ km s}^{-1}$ ,  $0.7 \pm 0.6 \text{ km s}^{-1}$  and  $0.6 \pm 0.4 \text{ km s}^{-1}$ , respectively. Overall there is no significant change in core bulk velocity. Note that the typical bulk velocity of Phase II cores is comparable to the bulk velocity of  $\sim 0.68 \text{ km s}^{-1}$  estimated for the coherent cores analyzed by Chen et al. (2019a). (The estimate presented by Chen et al. 2019a was a 1D velocity; here we take the isotropic assumption and uses a factor of  $\sqrt{3}$  to convert between the 1D and 3D velocities.) The result is also comparable to the “core-to-core” velocity derived for the dense cores in Perseus by Kirk et al. (2010). The physical properties are summarized in Table 1.

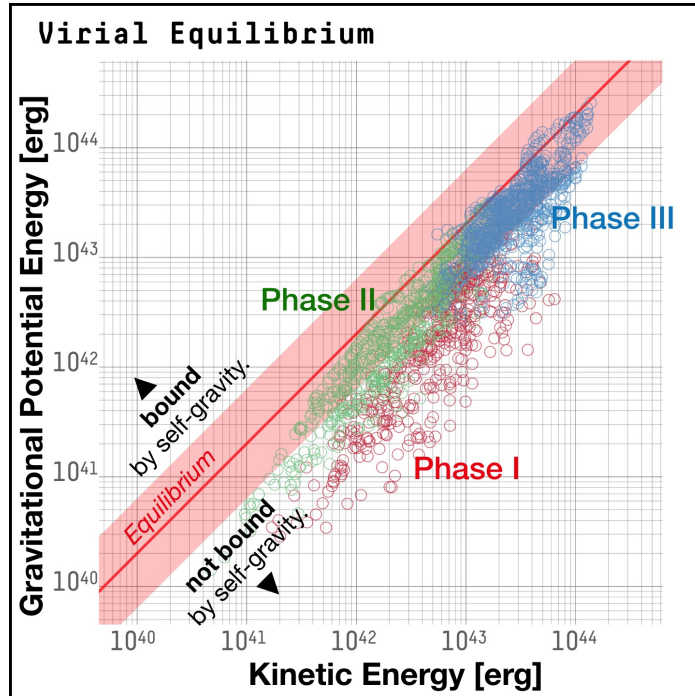


**Figure 11.** Distribution of the gravitational potential energy and the kinetic energy of structures in Phase I (red circles), Phase II (green circles) and Phase III (blue circles). The red band from the lower left to the top right marks the equilibrium between the gravitational potential energy and the internal kinetic energy (solid red line) within an order of magnitude (pinkish red band).

## 5. DISCUSSION

### 5.1. An Evolutionary Track for Cores

Based on the results presented in §4, we propose an evolutionary scenario where a core evolves through three distinct phases. Cores in these three phases bear characteristically different physical properties. In summary, the cores are “born” as turbulent density structures during Phase I. Most of these Phase I cores are not bound by self-gravity due to the relatively high level of turbulence within them. From Phase I to Phase II, the cores dissipate their turbulence, and coherent regions emerge within the cores. The dissipation of turbulence results in the core becoming more gravitationally bound. During Phase III, gravitational collapse occurs, and protostars start to form within the cores. The survival rates going from Phase I to Phase II and from Phase II to Phase III are  $\sim 55\%$  and  $\sim 84\%$ , respectively. There is also a non-zero fraction ( $\sim 7\%$ ) of Phase I cores that evolve directly into Phase III, and there is also a non-zero chance for Phase I and Phase II cores to dissipate ( $\sim 37\%$  and  $\sim 16\%$ , respectively; the percentages do not sum to 100% due to rounding). This constitutes a dynamic picture, where not all density structures become star-forming, but they do generally follow an evolutionary track going through these three phases.

Fig. 12a shows a schematic representation of the evolutionary track in a virial analysis. The variation in the masses and sizes of the Phase I cores is possibly the result of a combination of different turbulent modes and varying local physical conditions (e.g., as described by Burkert & Bodenheimer 2000; Hennebelle & Chabrier 2009; Hopkins 2013;

Padoan et al. 2019). Fig. 12b shows how this evolutionary track can explain previous observations of dense cores and coherent cores by situating the observed cores at different points along the evolutionary track.

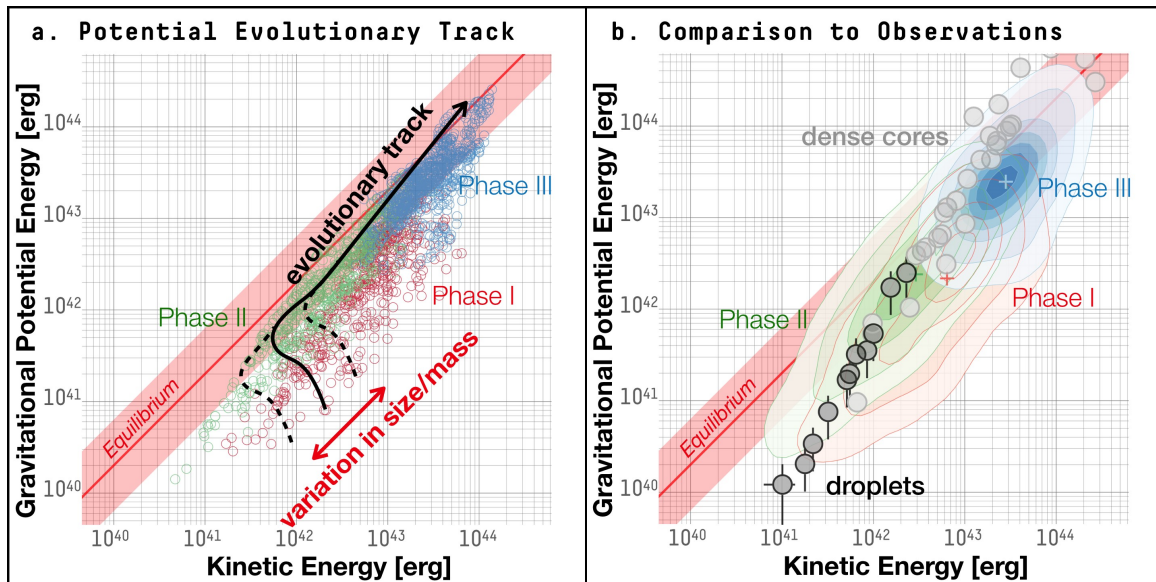


**Figure 12.** (a) Kinetic and gravitational potential energies, color coded by the clustering result discussed in §3.2. The black arrow shows a given track that connects the structures in each phase identified in §3.2. The red arrow shows that the starting point of a potential evolutionary track can vary depending on the initial mass and size of the structures. (b) Same as (a), with the distribution of cores in each phase shown as contours of constant posterior probabilities in a Gaussian kernel density estimation (KDE) analysis that estimates the underlying probability density function in this parameter space. The black dots are *droplets*, pressure-dominated coherent structures, observed by Chen et al. (2019a). The gray dots are dense cores from Goodman et al. (1993), most of which have turbulent velocity dispersions on the order of the sonic speed.

Despite the fact that many of the Phase I cores and some of the Phase II cores do not appear to be gravitationally bound in a virial analysis (Fig. 12a), the survival rates for Phase I cores to become Phase II cores and for Phase II cores to grow into star-forming Phase III cores are relatively high at  $\sim 55\%$  and  $\sim 84\%$ , respectively. Although the exact percentages for the survival rates likely depend on the cloud physical conditions, the fact that the cores not bound by self-gravity continue to evolve and may eventually become prestellar/protostellar is consistent with the observation of a substantial number of unbound coherent cores. Chen et al. (2019a) observed that these Phase II coherent cores, not bound by self-gravity, are instead confined by turbulent motions of the ambient gas. This confinement, provided by the turbulent pressure of the ambient gas, helps explain the relatively high survival rates. In general, when cores evolve from Phase I to Phase II, they move closer to a virial equilibrium. Future simulations with different parameters will be needed to explore how the survival rates depend on gas density, velocity dispersion and magnetic field.

Overall, the cores appear to transition smoothly between phases, and there is no discontinuous change in physical properties. As discussed above, the appearance and growth of the coherent region appears to be gradual, and that a core likely remains not bound by self-gravity in the early stages of Phase II. On the other hand, the transition between Phase II and Phase III seems to correspond to the disappearance of the coherent region within the core. However, we note that there is a certain degree of overlap and that some of the Phase III cores, including a number of the star-forming cores (with YSOs inside), still have coherent regions within them (Fig. 4). An observational example is the star-forming coherent core in the B5 region in Perseus, identified by Pineda et al. (2010). This coherent core is associated with a known YSO and contains at least three other starless substructures (Pineda et al. 2015). Pineda et al. (2010) observed an increase in velocity dispersion due to gravitational infall near the YSO in B5, which is also exhibited in some of the star-forming Phase III cores (Fig. 8).

Another criterion often used to distinguish between conventionally known starless and prestellar cores is gravitational boundedness. As shown in Fig. 12a, there is no sharp transition between gravitationally bound and unbound cores. There are Phase II cores that are gravitationally bound according to the virial analysis, and there are a few Phase III cores that are not gravitationally bound. Both the disappearance of the coherent region and the emergence of

gravitational boundedness are related to the onset of gravitational infall in our evolutionary picture. In this dynamic picture, one should not rely on the conventional virial analysis to predict whether a core will eventually form stars or not.

### 5.2. Comparison with Low-Mass Star and Core Formation Models

So, how does a core form in a molecular cloud, and how does core formation lead to the formation of stars? In this section we discuss three representative models of low-mass core and star formation and compare our results with these models.

First of all, starting with Padoan et al. (1997), a series of works have proposed turbulent fragmentation as the dominant mechanism in forming cores (Padoan et al. 1997; Padoan & Nordlund 2002; Hennebelle & Chabrier 2008, 2009; Hennebelle & Falgarone 2012; Hopkins 2013). In this model, structures develop in a “top-down” sense. Structures at smaller scales form when turbulent fluctuations in the “parent” larger-scale structure cause sub-regions to become gravitationally unstable. Hopkins (2013) suggests that the physical properties of cores formed via this mechanism are set at the time of fragmentation and are only weakly modified by the collapse process. In the Hennebelle & Chabrier (2008) model the decay of turbulence does not affect the “selection process,” which adopts gravitational instability as the criterion to “select” structures that continue evolving and eventually become prestellar/protostellar. In contrast, we find that the evolution of turbulence within the core plays an important role. As discussed in §5.1, turbulence dissipation in the first  $\sim 1 \times 10^5$  to  $2 \times 10^5$  years is necessary to reduce turbulent support before gravitational collapse starts. Although we do find that some Phase I cores are close to being gravitationally unstable and evolve directly into Phase III, we find that focusing only on density structures that are above the collapse threshold would bias the analysis by excluding cores that eventually become star-forming. However, based on our analysis, we agree that turbulent fluctuations are important in creating the initial distribution of density structures, although unlike in the theoretical framework of turbulent fragmentation, these density structures do not need to be initially gravitationally unstable to continue evolving to become prestellar cores.

Chen & Ostriker (2015) examine the formation of cores in post-shock layers of converging flows. They find that core contraction is anisotropic, and the material flow follows the direction of the magnetic field. They suggest that such anisotropic contraction along the field lines helps form gravitationally bound dense cores. On the other hand, they also find that filaments and dense cores form simultaneously in the post-shock layers. Overall, they suggest that shocks and the magnetic field play important roles in compressing gas to form prestellar cores, which allows subcritical clouds to form supercritical cores. While we do not examine the role of the magnetic field in detail in this work, we do find that many Phase I cores appear to be associated with shock-induced features. However, according to our analysis, these Phase I cores remain unbound by self-gravity for  $\sim 1 \times 10^5$  to  $2 \times 10^5$  years. As discussed above, the turbulence in Phase I cores continues to dissipate, and they become gravitationally unbound only after their turbulent velocity dispersion becomes subsonic. This disagrees with the model proposed by Chen & Ostriker (2014) and Chen & Ostriker (2015), where contraction makes a density structure gravitationally unstable during the initial stage of core formation. Similarly, while Chen & Ostriker (2015) find that the core mass and size are comparable to the critical Bonnor-Ebert mass and radius, most Phase I cores and some Phase II cores have density profiles shallower than a critical Bonnor-Ebert sphere. That is, these Phase I and Phase II cores are “subcritical” Bonnor-Ebert spheres. On the other hand, in agreement with the model proposed by Chen & Ostriker (2014) and Chen & Ostriker (2015), we also find that filaments and dense cores form simultaneously. Since almost all Phase I cores and many Phase II cores are not bound by self-gravity, we conclude that pressure plays an important role in confining these cores. This may also be related to the fact that the core properties examined by Chen & Ostriker (2015) are set by the total dynamic pressure, including magnetic and turbulent pressure, and the thermal sound speed and are independent of magnetic field strength and the pre-shock inflow velocity. Future works that examine the relation between cores in different phases and shocks/magnetic fields are needed.

Recently, Vázquez-Semadeni et al. (2017) and Ballesteros-Paredes et al. (2018) propose a gravity-regulated model of core formation, where dense cores form via “hierarchical gravitational fragmentation.” In the analytical model put forward by Ballesteros-Paredes et al. (2018), a star-forming core starts its evolution in a state of gravitational instability and remains gravitationally unstable throughout the evolution. Thus, a core in this model undergoes gravitational collapse at all times. Ballesteros-Paredes et al. (2018) propose that outside-in gravitational collapse generates the distribution of velocity dispersions observed in coherent cores, with larger velocity dispersions at larger radii and smaller velocity dispersions in the core centers. The simulated core in this model develops a density profiles similar

to the critical Bonnor-Ebert sphere, with  $\rho \propto r^{-2}$ . Based on our analysis, we conclude this model lacks the ability to explain the turbulence in Phase I cores and the dissipation of turbulence during Phase I and Phase II. In our analysis, when a core evolves from Phase II to Phase III, gravitational collapse starts at the center of the core (an “inside-out” collapse as proposed by [Shu 1977](#)), raising the velocity dispersion at the center above the thermal sonic speed first before increasing the gas dispersion towards the core edges. This can be seen in [Fig. 8](#), where many of the Phase III cores have centrally enhanced velocity dispersions. As discussed above, most Phase I cores and some Phase II cores have density profiles that are shallower than a critical Bonnor-Ebert sphere, although at later times, the profiles do approach Bonnor-Ebert-like profiles with  $\rho \propto r^{-2}$ . On the other hand, [Vázquez-Semadeni et al. \(2017\)](#) show that hierarchical gravitational fragmentation is capable of creating star-forming cores that have physical properties similar to those of the observed cores in a study of core formation in a molecular cloud undergoing global gravitational collapse in simulations. However, similar to the analytical model presented by [Ballesteros-Paredes et al. \(2018\)](#), the cores in the simulations studied by [Vázquez-Semadeni et al. \(2017\)](#) appear to be gravitationally supercritical at all times, while in our model, cores form as subcritical structures and evolve in a state of quasi-equilibrium for most of their lifetimes (see [Fig. 12](#)). The gravity-regulated model cannot fully explain the evolution of cores seen in our analysis.

In summary, the underlying difference between the model presented in this paper and previous theoretical models is the inclusion of gravitationally subcritical structures in the core evolution theory. In previous models, subcritical density structures are excluded in the analysis under the conventional assumption that such structures disperse before they can become prestellar/protostellar. Our model shows otherwise. As discussed in [§4.1](#), we find that a significant portion of cores that are not bound by self-gravity continue to evolve and eventually become prestellar/protostellar. Critically, turbulence dissipation appears to constitute a necessary and separate stage of core evolution that precedes gravitational collapse. Future studies that examine gravitationally subcritical cores along with supercritical ones are needed to understand the process of turbulence dissipation and how it sets the initial conditions for the later phase of gravitational collapse and star formation.

### 5.3. Core Formation and Filaments

Notably, in the simulations discussed above, filamentary structures form and evolve alongside cores. For examples, [Chen & Ostriker \(2015\)](#) find that filaments and cores form at the same time in the post-shock layer, and [Vázquez-Semadeni et al. \(2017\)](#) find that flows along filaments feed the clump that undergoes hierarchical collapse and form clusters of low-mass stars. There have also been a variety of theoretical studies particularly on the formation of cores within filaments, usually through fragmentation of the filaments (e.g., [Klessen 2001](#); [Burkert & Hartmann 2004](#); [Hennebelle & Chabrier 2009](#); [Vázquez-Semadeni et al. 2009](#); [Hopkins 2013](#); [Guszejnov & Hopkins 2015](#); [Padoan et al. 2019](#)).

In observation, fragmentation in filaments, often hierarchical in nature, has been observed toward both massive and low-mass star-forming regions (e.g., [Hacar & Tafalla 2011](#); [Palau et al. 2015](#); [Tafalla & Hacar 2015](#); [Beuther et al. 2015](#); [Ragan et al. 2015](#); [Henshaw et al. 2016](#); [Kainulainen et al. 2017](#); [Lu et al. 2018](#)). [Hacar et al. \(2013\)](#) observe a correlation between filamentary fragmentation and the formation of cores. Further studies of these cores by [Seo et al. \(2015\)](#) find that at least some of these cores have trans-/subsonic turbulent velocity dispersions and are likely confined by the pressure provided by the gas motions in the surrounding environment. Similarly, some of the coherent cores [Chen et al. \(2019a\)](#) identified are situated within filamentary structures.

Both observational and theoretical works find that the process of fragmentation within filaments depends on the properties of “sub-filaments” ([Hacar et al. 2013](#); [Smith et al. 2012, 2016](#)). A theoretical study by [Smith et al. \(2016\)](#) find that the formation of sub-filaments, sometimes known as “bundles,” have continuous distributions of velocities and form at the stagnation points of the turbulent velocity fields where shocks dissipate the turbulent energy. The same study also finds that depending on the gravitational criticality, some of these sub-filaments will likely fragment into star-forming cores, while others will not fragment but would still feed materials onto the embedded cores through accretion flows. [Suri et al. \(2019\)](#) characterize a correlation between material flows along the filaments and the formation of substructures within the filaments. A later study by [Chen et al. \(2020\)](#) finds that material flows onto and along the filaments and may help the accretion of the embedded star-forming cores at the converging points. Overall, both the fragmentation and the convergence of material flows appear to exist simultaneously within star-forming systems of the filamentary structures.

Using observational data, [Seo et al. \(2019\)](#) identify three different modes of star formation that depend on the locations of cores with respect to the filamentary structures. The “fast mode” occurs at the converging point of several

filamentary structures such as in a hub-filament system (Myers 2009) and forms a cluster of stars. On the other hand, the “slow mode” forms individual stars embedded within a filament. There is also an “isolated mode” where cores appear to be marginally stable and may undergo quasi-static evolution. In our simulation, we find that Phase I cores form both within the filamentary structures and also in isolation outside the filaments (Fig. 13). Many of the Phase I cores formed outside the filaments seem to be associated with shock-related features, and the ones that survive appear to move toward the dominant filamentary density structures. The shocks related to these Phase I cores may help the process of turbulence dissipation, as suggested by Smith et al. (2016). We find that many of these Phase I cores evolve into Phase II cores with substantial coherent regions within them before they reach the nearby denser filaments. Then, it is within these filaments that they become bound by self-gravity and actively accrete mass (Phase III). For cores within filaments, Chen & Ostriker (2015) suggest that the shocks driven by converging turbulent flows can help form high-density structures, which may explain the formation of Phase I cores within filamentary structures. In our simulation, we find that Phase I cores formed within filaments mostly stay within the filaments and evolve into Phase II/III cores there.

Fig. 13 shows that the regions most crowded with cores are near filamentary structures. Combined with the fact that Phase III star-forming cores are found in more clustered regions compared to Phase I/II cores (see Fig. 14), the spatial distribution of cores is consistent with the formation of Phase I cores both within and outside the filaments. This is also consistent with the fact that many Phase I cores evolve into Phase II cores before they reach the denser filamentary structures but rarely evolve into Phase III star-forming cores outside the high-density and usually more crowded regions. Future studies of the relation between cores and filaments are needed to understand the detailed physical processes involved in the formation and evolution of cores in the context of structure formation within filaments and molecular clouds.

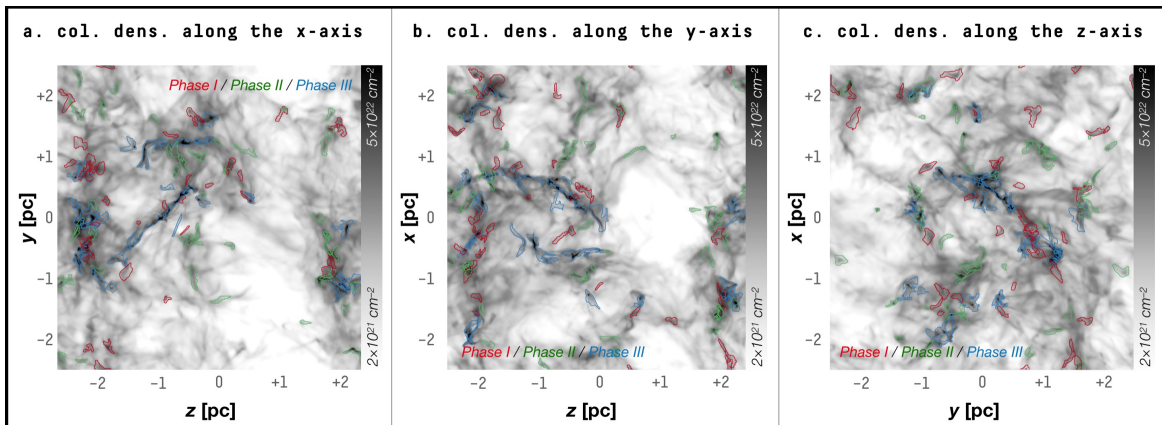


**Figure 13.** Maps of column density integrated along the (a) x-axis, the (b) y-axis and the (c) z-axis of the simulated box. The contours mark the boundaries of dendrogram leaves corresponding to the Phase I (red), Phase II (green) and Phase III (blue) cores. The snapshot is taken at  $t = 5 \times 10^5$  yr.

#### 5.4. Comparison with high-mass star formation models

Our simulation represents typical nearby low-mass star-forming regions, like Perseus, Ophiuchus and Taurus, with similar gas temperatures, column densities and velocity dispersions. Likewise, the simulated core properties, including masses and sizes, are similar to those of cores identified in these regions. This reinforces that our proposed core evolution model is applicable in the context of low-mass star formation as defined by stars with masses below a few solar masses. High-mass star formation, which is characterized by higher gas temperatures, velocity dispersions, column densities and stellar densities, may proceed very differently and not pass through the phases we propose here. However, observations suggest star formation exists on a continuum, low and high-mass star formation occurs co-spatially and contemporaneously, and there is not necessarily a clear dichotomy between them. To date, no coherent cores with high masses that could be progenitors of massive stars have been observed. This may be because such cores are distant and rare or because few, if any, massive starless cores exist (Tan et al. 2014). However, our evolutionary model shares some characteristics with several models for high-mass star formation, as we discuss here. During Phase

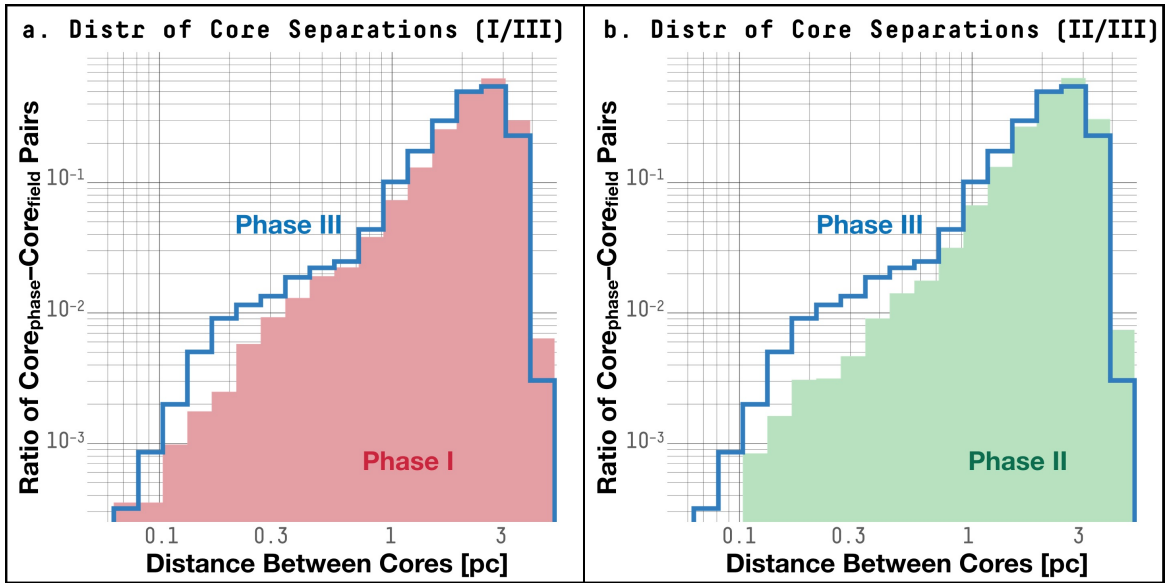


**Figure 14.** Histograms of the core separation between a core in one of the three phases and its nearest neighbor. Note that to investigate how crowded the environment is, we do not limit the nearest neighbor to be a core of the same phase. (a) Histograms of core separations for Phase I (red shaded area) and Phase III (blue line). The height of the histogram is the ratio of core-core pairs, with one of the core in the indicated phase and the other in the general core population. (b) Same as (a), but for Phase II (green shaded area) and Phase III (blue line).

I cores are trans-to-supersonically turbulent and appear to be supported by turbulent pressure, characteristics that are adopted as the initial conditions of massive cores in the “turbulent core” (TC) model for high-mass star formation (McKee & Tan 2002, 2003). In this model, turbulence provides internal pressure support and mediates gravitational collapse. Later work notes that strong magnetic fields may also contribute to the stability of massive cores (Tan et al. 2013). However, the TC model does not address in detail how such cores form. The challenge of identifying truly massive, starless cores and the apparent rarity of such objects suggest that some degree of collapse and star formation proceeds before a large reservoir of gas accumulates (Padoan et al. 2019). In other words, massive star formation is contemporaneous with massive core formation. In our model a significant portion of the core mass accumulates before the internal turbulence decays and collapse proceeds. However, the higher masses of Phase III cores indicates that some degree of core growth continues during the collapse phase.

In the opposite extreme, the competitive accretion (CA) model predicts that cores as discrete objects are relatively unimportant to the final outcome of star formation (Zinnecker 1982; Bonnell et al. 2001a,b). Instead, massive stars form at the center of clouds within the largest gravitational potential well, which funnels material inwards and facilitates high stellar accretion rates. In this case, core masses are independent of the final masses of the stars that form within them, and massive starless cores never exist (Smith et al. 2009; Mairs et al. 2014). The CA model stresses the importance of the local environment and role of neighboring stars. In our model, cores form both outside and inside filamentary regions, where the latter has the greatest ability for cores (and protostars) to grow due to inflowing gas. We find that Phase III cores tend to have closer near-neighbors (see Fig. 13) and higher masses, suggesting that environment has some influence on the progression of core evolution. The difference in clustering between Phase I/II cores and Phase III cores may be in part because some fraction of cores disperse before reaching Phase III, which could be more likely to occur if their local environment does not allow sufficient mass accretion to trigger collapse. However, we note that cores form in both clustered and isolated regions and, given the similarity between the distributions in Fig. 13, the environment appears to play a relatively minor role, at least for low-mass star formation. Future studies of simulations that include outflows are needed to fully understand the effects of possible interactions between cores in the more crowded environment.

Recently, Padoan et al. (2019) proposed the inertial-inflow model, in which massive stars form in turbulent regions characterized by large-scale converging flows. The inertial-inflow model is formulated by analyzing magnetized, driven turbulent simulations not too dissimilar from the one we analyze here, although Padoan et al. (2019) follow a larger spatial volume and do not resolve the formation of low-mass stars ( $M_* \lesssim 2 M_\odot$ ). Turbulent fragmentation produces

the initial core properties and sets their growth timescale; massive stars form in cores that continue to grow through accretion. This model predicts that truly massive starless cores do not exist, since collapse begins before a significant amount of mass accumulates. Of the high-mass models we discuss here, the inertial-inflow model is the most similar to the one we propose for low-mass star formation, namely, in that it emphasizes the role of shocks and filaments in core formation and growth. However, it does not explicitly address the early stages of core formation, and the cores identified in the simulation are gravitationally bound by construction, so they are analogous to our Phase III cores. It seems possible that the cores follow the phases we propose here and the inertial-inflow model represents a natural extension of our core evolution model to higher masses. Future work is required to determine whether high-mass cores proceed through a coherent phase prior to being gravitationally bound.

### 5.5. Observational Effects

Here we compare the simulations with the density and velocity dispersion profiles of the coherent cores identified by Chen et al. (2019a), including with the droplets, which are not bound by self-gravity. We infer the PCA components of the observed coherent cores by first computing a new, *observed* PCA transformation using the density and velocity dispersion profiles of the simulated cores *convolved with a Gaussian beam* of the same size as the beam of the GAS observations with added uncertainties equivalent to the uncertainties of the column density and velocity dispersion measurements, respectively (Friesen et al. 2017; Chen et al. 2019a). We use the observed PCA transformation to position the observed coherent cores in the *observed* PCA space. We find the  $n$  simulated cores identified in the simulation closest to each of the observed cores, using the Euclidean distance in the *observed* PCA space. We then position each observed core at the average position of these  $n$  simulated cores in the original PCA space (shown in Fig. 4). Here we use  $n = 15$  ( $\sim 0.7\%$  of the total number of cores identified in the simulation), and the result is shown in Fig. 15. We see that the inferred positions of the observed cores are consistent with the results presented by Chen et al. (2019a), where these cores are identified as coherent structures with different levels of gravitational boundedness.

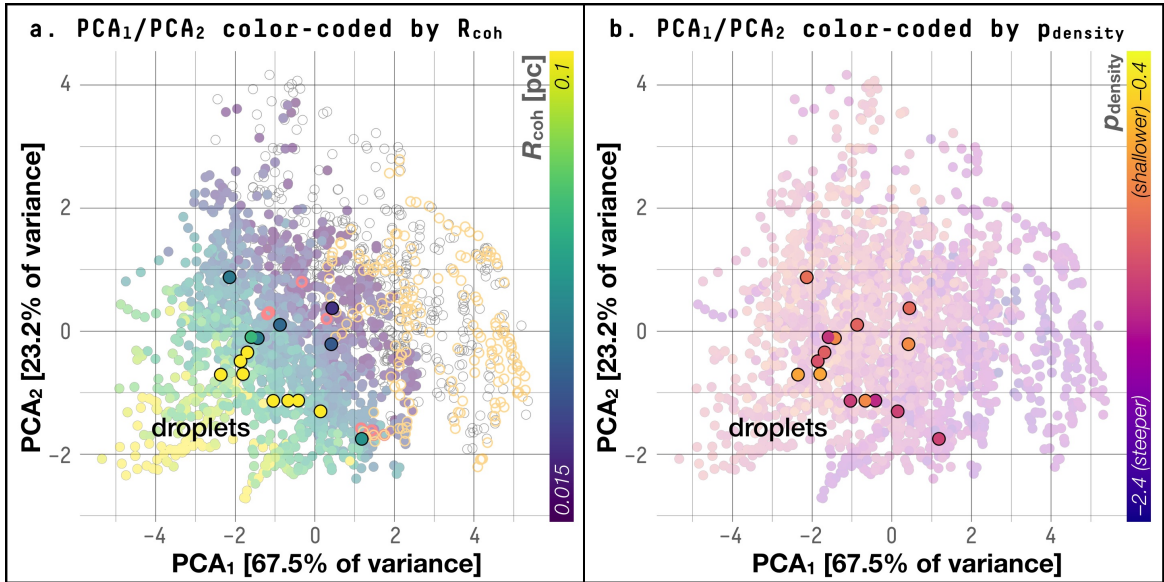


**Figure 15.** Same as Fig. 4, overlaid with the coherent cores observed by Chen et al. (2019a). (a) Distribution of the first and second PCA components of the coherent cores observed by Chen et al. (2019a) (solid colored dots) and all independent structures in the simulation (transparent colored dots), color coded by the size of the coherent region defined as the region within which the turbulence is subsonic. (b) Same as (a), but the data points are color coded by the index of the power law fitted to the radial density profile of each structure.

Intriguingly, coherent cores have only been directly observed and resolved using observations of  $\text{NH}_3$  hyperfine line emission. Meanwhile, there are observations of  $\text{C}^{18}\text{O}$  and  $\text{N}_2\text{H}^+$  molecular line emission that either did not resolve the transition to coherence and/or probed only the interior of a coherent core (Goodman et al. 1998; Caselli et al. 2002). Using the density and velocity dispersion profiles reconstructed from the PCA analysis, it is possible to examine the limits of observations to detect different phases of cores. There are a number of factors that may affect the ability of an

observation in detecting cores. An easy way to define the observational limits in the PCA space is to estimate the size of a core as observed between the detection threshold and the saturation threshold. The detection threshold involves a combination of the physical conditions an observational tracer probes and the maximum sensitivity the observation achieves. The saturation threshold is determined by the physical conditions for which the molecular species no longer emits (e.g., due to depletion onto dust grains; Goldsmith 2001; Draine 2003) and/or when the emission line becomes optically thick. Phase III cores are relatively easier to detect. They are expected to be denser and more chemically evolved, providing a larger selection of possible molecular line tracers. Probing the internal velocity structures of Phase III cores is usually limited by the saturation threshold, and choosing the right molecular line tracer becomes critical. Numerous examples of prestellar and protostellar cores that likely correspond to this phase in the simulations have been identified in observations (Tafalla et al. 2004; Enoch et al. 2008; Kauffmann et al. 2008; Rosolowsky et al. 2008a; Belloche et al. 2011). At an even later stage, the formation of YSOs within cores provides an extra observational hint that they belong to Phase III such as excess infrared emissions and molecular outflows (Bontemps et al. 1996; Arce et al. 2007).

To probe Phase II coherent cores and resolve the transition to coherence at their boundaries, we must take into account the size of the coherent region and the physical conditions under which the transition to coherence occurs. By comparing Figs. 7 and 8, we see that the transition to coherence generally corresponds to a density threshold of  $\geq 2 \times 10^4 \text{ cm}^{-2}$  and that the maximum density rarely exceeds  $10^5 \text{ cm}^{-2}$  in Phase II cores. Fig. 16 shows the range of the PCA space that is “observable” (i.e., detectable and resolvable) by two observations of different resolutions tracing different density ranges (unshaded areas), as well as the sizes of the coherent regions (red contours). These ranges are based on calculations of the projected size of a structure between the detection threshold and the saturation threshold. The observation shown in Fig. 16a is similar to the observations of  $^{13}\text{CO}$  (1-0) molecular line emission by a telescope similar to the Five College Radio Astronomy Observatory (FCRAO), assuming a distance of 137.3 pc, which is the distance of the Ophiuchus molecular cloud (e.g., the observations included in the Coordinated Molecular Probe Line Extinction and Thermal Emission (COMPLETE) Survey; Ridge et al. 2006; Ortiz-León et al. 2017; Zucker et al. 2019). In comparison, the observation limits shown in Fig. 16b are similar to observations of the  $\text{NH}_3$  (1, 1) hyperfine line by a telescope such as the GBT, again assuming a distance similar to that of Ophiuchus (e.g., GAS observations; Friesen et al. 2017). The figure suggests that GBT observations are ideal for probing both Phase I and Phase II cores. In particular, such observations probe Phase II coherent cores and resolve the transition to coherence at the same time, as done by Pineda et al. (2010) and Chen et al. (2019a) in their analyses of the only known examples of directly resolved coherent cores. Molecular line tracers that are also sensitive to lower densities would make the observed line widths appear broader due to the turbulent motions of the lower-density materials along the line of sight. Molecular line tracers tracing higher densities would resolve the interior of the coherent region but not the transition to coherence occurring at  $\geq 2 \times 10^4 \text{ cm}^{-2}$  at the same time (this may be the case for the  $\text{N}_2\text{H}^+$  observations performed by Caselli et al. 2002).

Phase I is the only phase among the three in our proposed scenario of core evolution where there is no clear observational counterpart. There are two possible reasons no Phase I counterpart exists. One is because Phase I cores are less dense and more turbulent. Thus, they are usually not bound by self-gravity. They do not have identifiable coherent regions, and they do not show clear signs of star formation like the prestellar and protostellar cores. This could cause the Phase I cores to be missed in previous observations. To check this possibility, we revisit the GAS DR1 data and the Herschel column density maps, since Fig. 16b suggests that these observations are able to identify the Phase I cores. We look for independent structures on the maps of  $\text{NH}_3$  (1, 1) peak brightness temperature and Herschel column density in all four regions included in the GAS DR1 (L1688, B18, NGC1333 and Orion A; see Figs. 4 to 7 in Friesen et al. 2017). Since Phase I cores are not expected to have coherent regions nor YSOs within them, we exclude structures with subsonic turbulent velocity dispersions and those with YSO(s) inside. We also exclude structures that are bound by self-gravity, since Phase I cores are not expected to be gravitationally bound. After applying these criteria, we find no structures that resemble Phase I cores, although we note that Phase I cores may still be hidden by false density enhancements due to multiple line-of-sight density structures.

Another possible reason that we do not identify Phase I cores in the GAS DR1 data may be the formation timescale of  $\text{NH}_3$ . Compared to carbon-bearing molecular species like CCS and  $\text{HC}_n\text{N}$ ,  $\text{NH}_3$  forms relatively late. According to Suzuki et al. (1992), the timescale for the abundance of  $\text{NH}_3$  to reach an  $\text{NH}_3$ -to- $\text{H}_2$  abundance level of  $10^{-8.5}$  to  $10^{-8.0}$  typical of the GAS DR1 data for a density range between  $10^4 \text{ cm}^{-3}$  and  $10^5 \text{ cm}^{-3}$  is  $\geq 4 \times 10^5 \text{ yr}$ . In comparison, the typical Phase I timescale is  $\sim 1.4 \times 10^5 \text{ yr}$ . It is likely that the abundance of  $\text{NH}_3$  remains relatively low during Phase

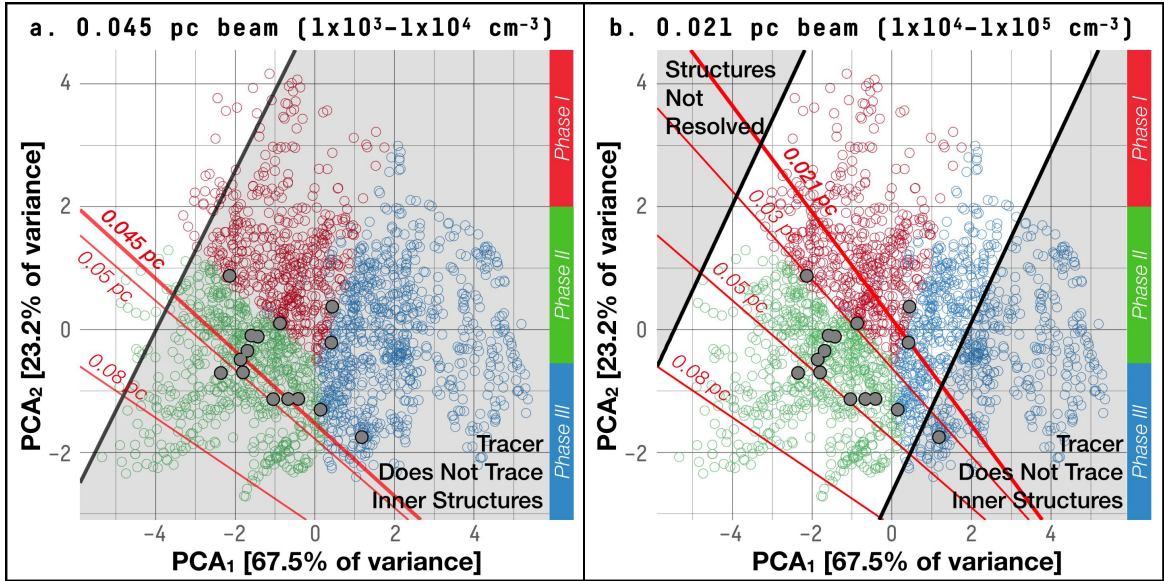


**Figure 16.** Same as Fig. 5, shown with the range of the PCA space that can be observed and the corresponding sizes of coherent regions based on reconstructed profiles. (a) The range of the PCA space that can (unshaded) and cannot (shaded) be observed by an observation with a beam size corresponding to 0.045 pc of a molecular line tracer tracing the density range between  $1 \times 10^3 \text{ cm}^{-2}$  and  $1 \times 10^4 \text{ cm}^{-2}$ . The sizes of the coherent regions within the reconstructed profiles in the PCA space are indicated by the thin red contours, with the thick red line contouring the range of the PCA space where the reconstructed profiles have coherent regions larger than the beam size (toward the bottom left of the thick red line). The solid gray dots correspond to the coherent cores observed by Chen et al. (2019a), and the structures in the simulation are the colored circles coded by the evolutionary phase they belong to. This mimics the limits of CO observations, such as those included in the COMPLETE Survey. (b) Same as (a), with the range of the observable PCA space now corresponding to an observation with a beam size of 0.021 pc for a molecular line tracer tracing the density range between  $1 \times 10^4 \text{ cm}^{-2}$  and  $1 \times 10^5 \text{ cm}^{-2}$ . This mimics the limits of  $\text{NH}_3$  observations, such as those included in the GAS DR1.

I. However, the formation of  $\text{NH}_3$  could have started earlier than the Phase I starting time, which depends on our definition of a Phase I structure. As described in §3.1, we require a density structure to have a size larger than  $\sim 0.028$  pc above a density threshold of  $10^4 \text{ cm}^{-3}$  to be identified as a core. In reality, the growth of a density structure in the molecular cloud starts before our definition of the beginning of Phase I. It can take roughly one free-fall time,  $t_{\text{ff}} = \sqrt{3\pi/32G\rho}$ , for gas to grow into a structure that would be captured by our identification criteria (see §3.1), which defines the Phase I starting point. For a density of  $10^4 \text{ cm}^{-3}$ , the free-fall time is  $\sim 3.1 \times 10^5$  yr. If the formation of  $\text{NH}_3$  begins when the density growth starts, then the timescale estimates are consistent with the lack of Phase I detections and the fact that Chen et al. (2019a) observed  $\text{NH}_3$  toward early Phase II coherent cores that are not bound by self-gravity. In this case, Phase I cores may show up as structures on the Herschel column density maps but not in the maps of  $\text{NH}_3$  peak brightness temperature. Unfortunately, the detection of  $\text{NH}_3$  is needed to derive the velocity profile.

Future observations hunting for Phase I cores would ideally consist of a tracer such as dust emission or dust extinction that is sensitive to a larger range of column density than most of the molecular line tracers (Goodman et al. 2009a). The observations would also include molecular species that are expected to form at an earlier time during core evolution. According to Suzuki et al. (1992), candidate “early-time tracers” include carbon-bearing molecules such as CCS and  $\text{HC}_n\text{N}$ . Intriguingly, CCS and  $\text{HC}_5\text{N}$  molecular line emission is detected in and around the coherent cores identified in B18 but not around the coherent cores in L1688 (Friesen et al. 2017). There is also no detection of CCS and  $\text{HC}_5\text{N}$  in NGC 1333 and Orion A. There may be a period of time in the evolution of cores when these species coexist with  $\text{NH}_3$ . Further chemical modeling is required to select the best molecular line tracers to identify Phase I cores.

## 6. CONCLUSIONS

We present a method to identify, track and characterize the evolution of dynamic gas structures in simulations. Our method is general and is applicable to other numerical models of star formation. Unlike many previous core identification and analysis methods, we do not make *a priori* assumptions about the physical properties of the cores or

their density and velocity dispersion distributions. This is done with the help of PCA decomposition and the  $k$ -means clustering algorithm. To provide a complete picture of core formation and evolution that links turbulent molecular clouds to star-forming cores, we study the formation, evolution and collapse of dense cores identified in an MHD simulation. We identify all independent density structures above  $10^4 \text{ cm}^{-3}$  in the simulation using the dendrogram algorithm. We utilize unsupervised machine learning techniques, PCA and the  $k$ -means clustering algorithm, to analyze the full density and velocity dispersion profiles. We then track the cores as they evolve and move across both the simulation and the PCA space. As a result, we find there exists a core evolutionary sequence consisting of three distinct phases. Phase I corresponds to the formation of turbulent density structures in the molecular cloud. Phase I cores have turbulent internal velocity dispersions and shallower density profiles, and they remain largely not bound by self-gravity. Phase II corresponds to the dissipation of turbulence and the formation of coherent regions, defined as a region with subsonic and nearly uniform velocity dispersion, within the cores. Phase II cores resemble observed coherent cores, including ones that are not bound by self-gravity like the droplets observed by [Chen et al. \(2019a\)](#). Phase III cores are characterized by gravitational infall, which dominates the internal dynamics. Phase III cores include both gravitationally bound prestellar and protostellar cores.

We estimate typical lifetimes of  $1.4 \pm 1.0 \times 10^5 \text{ yr}$ ,  $3.3 \pm 1.4 \times 10^5 \text{ yr}$  and  $3.3 \pm 1.4 \times 10^5 \text{ yr}$ , respectively, for Phase I, II and III. Although Phase I cores are mostly not bound by self-gravity, 55% of Phase I cores continue evolving to become Phase II cores, while another 7% of Phase I cores directly evolve to become Phase III cores. We also find that 84% of Phase II cores evolve to become Phase III cores. This evolution explains the distribution of observed dense cores in a virial analysis, with variation in the initial physical properties of Phase I cores explaining the spread of the distribution (see Fig. 12).

We find that Phase I cores form both within denser filamentary structures and in isolation outside the filaments. Many of the isolated Phase I cores appear to be associated with shock-related features. These Phase I cores can evolve to become Phase II cores before they reach dense filamentary structures. Meanwhile, filamentary fragmentation and the convergence of material flows appear to act simultaneously in the denser and more clustered environment within the filaments, where most of the Phase III cores are found. Future study of the relation between core evolution and filaments will examine how different processes affect the physical properties of the cores.

We show that the coherent cores observed by [Chen et al. \(2019a\)](#) are consistent with the Phase II regime using the same PCA transformation derived for the cores in the simulation. We also demonstrate that the observations of  $\text{NH}_3$  hyperfine line emission with a physical resolution of  $\sim 0.2 \text{ pc}$  or finer, like the ones carried out by [Friesen et al. \(2017\)](#), are ideal for detecting Phase II cores. Similar observations are expected to also probe Phase I cores. However, we cannot identify any in the GAS DR1 data. This is likely because the formation timescale of  $\text{NH}_3$  is longer than the typical lifetime of Phase I cores, and we propose that observations of early-time high-density tracers such as  $\text{CCS}$  and  $\text{HC}_n\text{N}$  are needed in order to probe Phase I cores in the future.

This work was supported by a Cottrell Scholar Award and NSF Career Grant AST1650486.

*Facilities:* GBT (KFP+VEGAS), Herschel Space Observatory (PACS+SPIRE)

*Software:* astropy ([The Astropy Collaboration et al. 2018](#)), Glue ([Beaumont et al. 2015](#); [Robitaille et al. 2017](#)), PySpecKit ([Ginsburg & Mirocha 2011](#)), RADMC-3D ([Dullemond et al. 2012](#))

## APPENDIX

### A. COMPARISON WITH T-DISTRIBUTED STOCHASTIC NEIGHBOR EMBEDDING (T-SNE) METHOD

In this appendix, we compare the PCA analysis with another popular representation learning algorithm, the t-distributed stochastic neighbor embedding (t-SNE) method. t-SNE is a manifold algorithm that represents the affinities in the original (data) space by Gaussian distributions and the affinities in the embedded (lower-dimensional) space by Student's t-distributions. It was first formulated and put into practice by [van der Maaten & Hinton \(2008\)](#). Manifold algorithms like t-SNE are non-linear dimensionality reduction algorithms, and in a way, they can be seen as extensions of linear dimensionality reduction algorithms such as PCA. Manifold algorithms like t-SNE are designed to capture non-linear structures in data. T-SNE has enjoyed popularity in industry and shows its strength by outperforming other manifold algorithms in standard tasks such as the recognition of hand-written digits in the Modified National

Institute of Standards and Technology (MNIST) dataset (van der Maaten & Hinton 2008). Its application in analyses of astronomical data has recently been studied by Traven et al. (2017) and Anders et al. (2018), where t-SNE was utilized in identifying structures in spectral data. By design, t-SNE is expected to perform better than PCA on identifying non-linear features and local clustering structures in the input data.

t-SNE optimizes the Kullback-Leibler (KL) divergence between the Gaussian joint probabilities representing the affinities between data points in the original space and the Student’s t-distributions representing the affinities between data points in the embedded space. As a result, t-SNE projects the original data into the embedded space and visualizes the structures in the original dataset through clusterings in the embedded space. By design, t-SNE equalizes distances between data points belonging to the same cluster, and thus, the distances in the embedded space between data points in the same cluster are not necessarily meaningful. That is, the size of a cluster in the embedded space is not directly correlated with the variance in the data points belonging to the cluster. In addition, the distances *between* clusters in the embedded space are not necessarily meaningful, in the sense that clusters separated by larger distances are not necessarily more different than clusters separated by smaller distances. In summary, t-SNE is an algorithm designed to separate clusters in the embedded space instead of providing an absolute measurement of variances between and within the clusters. Note that this is different from PCA, where the variances in the original data set are projected into the embedded space.

The ability of t-SNE to capture the global geometry in the original dataset strongly depends on the choice of a hyperparameter called “perplexity,” which controls the size of Gaussian distributions used to represent the affinities between data points in the original space. For a data point,  $x_i$ , t-SNE uses a Gaussian distribution centered at  $x_i$  to give the probability in selecting the nearest neighbors when embedding the dataset. By this definition, the probability of selecting another data point,  $x_j$ , is the Gaussian probability  $P_i(x_j) \sim N_i(x_j)$ . The perplexity of this Gaussian distribution,  $P_i(x)$ , is defined as  $perp(P_i) = 2^{H(P_i)}$ , where  $H(P_i)$  is the Shannon entropy defined as the expected value of  $-\log_2 P$  over all other data points,  $H(P_i) = -\mathbb{E}_{x_j \neq x_i}[\log_2 P_i(x)]$ .  $-\log_2 P(x)$  is sometimes known as the *self-information* and measures the “amount of information” in an event  $x$ . Roughly speaking, the perplexity controls the balance of t-SNE’s attention between local and global structures. Smaller values of perplexity make t-SNE more sensitive to local structures, while larger values of perplexity make t-SNE more sensitive to global structures. The choice of perplexity depends on the problem, and there is no simple mathematical prescription for choosing the best value.

Figs. 17, 18 and 19 show t-SNE distributions derived using different values of perplexity. Unlike PCA, each run of t-SNE with the same setup parameters produces different embedded distributions. The embedded distribution also depends on hyperparameters such as the number of iterations and the learning rate. Here we determined the number of iterations and the learning rate by observing the KL divergence to make sure that each run has reached stability. For each value of perplexity, we ran t-SNE 100 times and chose the embedded distribution with the lowest KL divergence. Consistent with the definition of perplexity, t-SNE identifies multiple local clusters for a perplexity of 5. As shown in the figures, such local clusters almost entirely disappear when we increased the perplexity to 100. Intermediate values of perplexity produce distributions that seem to identify clusters with the most distinct physical properties, such as the cores with the largest coherent regions or the cores with active star formation. This is particularly obvious for perplexity values of 50 and 80 (see Figs. 17 and 18).

Overall, we find with the “right” range of perplexity, t-SNE results preserve the core phases as well as the distribution of cores in the PCA space. There could potentially be more local structures in the t-SNE distributions that are not captured by PCA, since the t-SNE distributions look much clumpier than the PCA distribution even with large values of perplexity. However, one caveat of t-SNE is that it may falsely identify non-existent structures when the perplexity is ill-chosen (e.g., t-SNE identifies localized structures in Gaussian distributed data sets when low values of perplexity are used; van der Maaten & Hinton 2008). A more detailed analysis is required before we can fully utilize t-SNE and take advantage of its ability to identify non-linear structures in continuously distributed datasets such as the density and velocity dispersion profiles analyzed in this paper.

## REFERENCES

- Alves, J. F., Lada, C. J., & Lada, E. A. 2001, *Nature*, 409, 159
- Anders, F., Chiappini, C., Santiago, B. X., et al. 2018, *A&A*, 619, A125, doi: [10.1051/0004-6361/201833099](https://doi.org/10.1051/0004-6361/201833099)

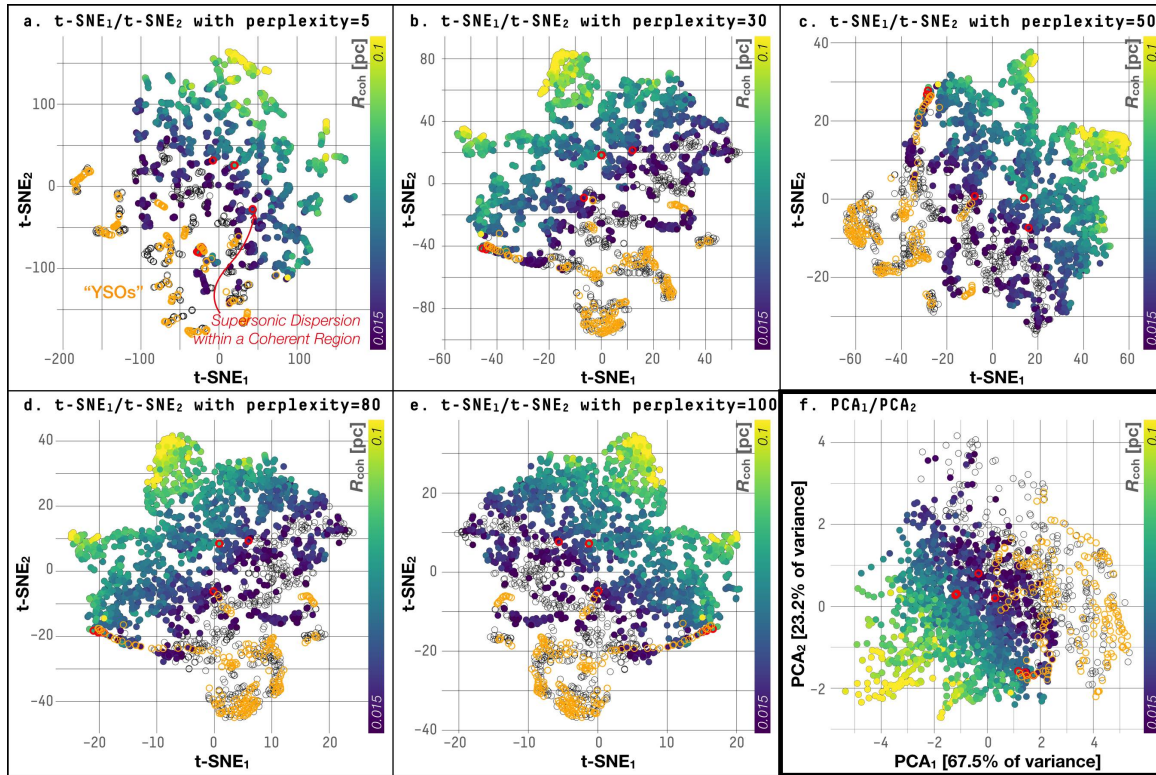


**Figure 17.** Distribution of t-SNE components compared to the distribution of the first two PCA components, color coded by the size of the coherent regions. The empty circles are the cores without coherent regions, and the yellow circles mark the cores with YSOs within them. The red circles mark the cores that show supersonic turbulent velocity dispersion around the center of their coherent regions. Distribution of t-SNE components derived with a perplexity of (a) 5, (b) 30, (c) 50, (d) 80 and (e) 100. (f) Distribution of the first two PCA components. This panel shows the same plot as in Fig. 4a.

- André, P., Men'shchikov, A., Bontemps, S., et al. 2010, *A&A*, 518, L102
- Arce, H. G., Shepherd, D., Gueth, F., et al. 2007, in *Protostars and Planets V*, ed. B. Reipurth, D. Jewitt, & K. Keil, 245
- Ballesteros-Paredes, J., Vázquez-Semadeni, E., Palau, A., & Klessen, R. S. 2018, *MNRAS*, 479, 2112, doi: [10.1093/mnras/sty1515](https://doi.org/10.1093/mnras/sty1515)
- Barranco, J. A., & Goodman, A. A. 1998, *ApJ*, 504, 207, doi: [10.1086/306044](https://doi.org/10.1086/306044)
- Beaumont, C., Goodman, A., & Greenfield, P. 2015, in *Astronomical Society of the Pacific Conference Series*, Vol. 495, *Astronomical Data Analysis Software and Systems XXIV (ADASS XXIV)*, ed. A. R. Taylor & E. Rosolowsky, 101
- Belloche, A., Parise, B., Schuller, F., et al. 2011, *A&A*, 535, A2, doi: [10.1051/0004-6361/201117276](https://doi.org/10.1051/0004-6361/201117276)
- Beuther, H., Ragan, S. E., Johnston, K., et al. 2015, *A&A*, 584, A67, doi: [10.1051/0004-6361/201527108](https://doi.org/10.1051/0004-6361/201527108)
- Bonnell, I. A., Bate, M. R., Clarke, C. J., & Pringle, J. E. 2001a, *MNRAS*, 323, 785, doi: [10.1046/j.1365-8711.2001.04270.x](https://doi.org/10.1046/j.1365-8711.2001.04270.x)
- Bonnell, I. A., Clarke, C. J., Bate, M. R., & Pringle, J. E. 2001b, *MNRAS*, 324, 573, doi: [10.1046/j.1365-8711.2001.04311.x](https://doi.org/10.1046/j.1365-8711.2001.04311.x)
- Bonnor, W. B. 1956, *MNRAS*, 116, 351, doi: [10.1093/mnras/116.3.351](https://doi.org/10.1093/mnras/116.3.351)
- Bontemps, S., André, P., Terebey, S., & Cabrit, S. 1996, *A&A*, 311, 858
- Burkert, A., & Alves, J. 2009, *ApJ*, 695, 1308, doi: [10.1088/0004-637X/695/2/1308](https://doi.org/10.1088/0004-637X/695/2/1308)
- Burkert, A., & Bodenheimer, P. 2000, *ApJ*, 543, 822, doi: [10.1086/317122](https://doi.org/10.1086/317122)
- Burkert, A., & Hartmann, L. 2004, *ApJ*, 616, 288, doi: [10.1086/424895](https://doi.org/10.1086/424895)
- Burkhart, B., Lazarian, A., Goodman, A., & Rosolowsky, E. 2013, *ApJ*, 770, 141, doi: [10.1088/0004-637X/770/2/141](https://doi.org/10.1088/0004-637X/770/2/141)
- Caselli, P., Benson, P. J., Myers, P. C., & Tafalla, M. 2002, *ApJ*, 572, 238, doi: [10.1086/340195](https://doi.org/10.1086/340195)
- Chen, C.-Y., & Ostriker, E. C. 2014, *ApJ*, 785, 69, doi: [10.1088/0004-637X/785/1/69](https://doi.org/10.1088/0004-637X/785/1/69)
- . 2015, *ApJ*, 810, 126, doi: [10.1088/0004-637X/810/2/126](https://doi.org/10.1088/0004-637X/810/2/126)
- . 2018, *ApJ*, 865, 34, doi: [10.3847/1538-4357/aad905](https://doi.org/10.3847/1538-4357/aad905)

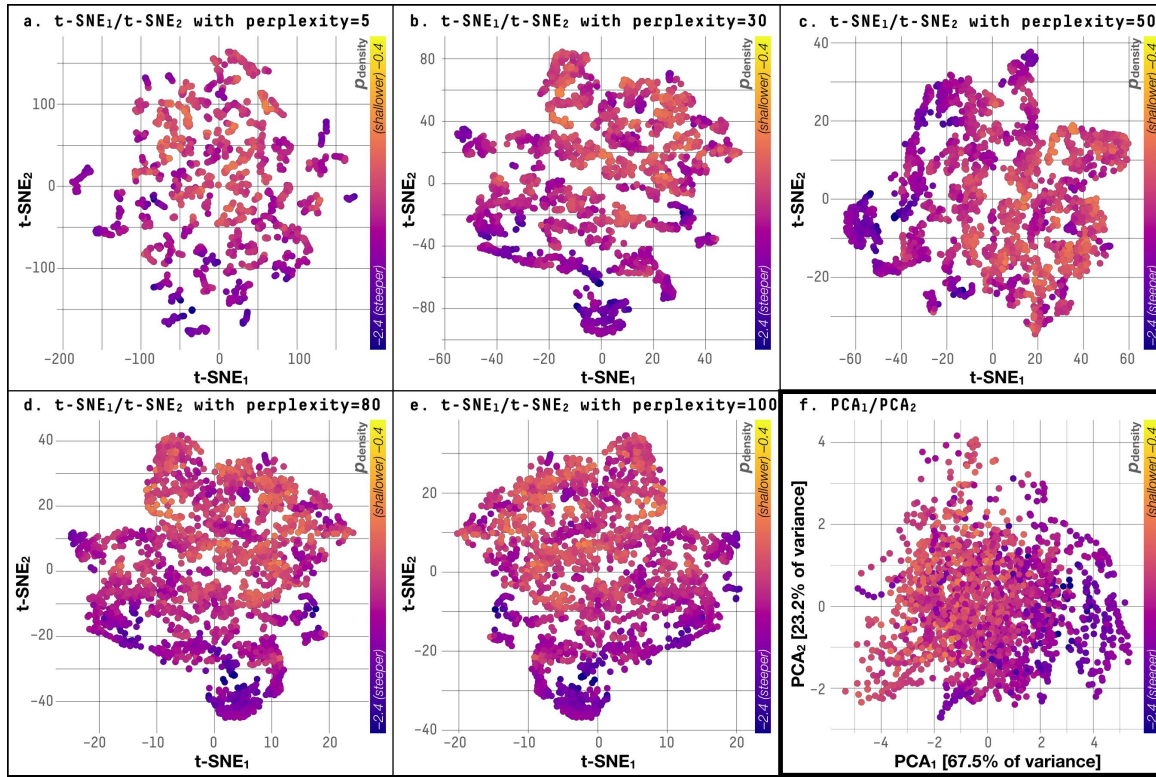


**Figure 18.** Same as Fig. 17, but the data points are color coded by the indices of the power-law fits to the core density profiles. The t-SNE distributions are derived with perplexity of (a) 5, (b) 30, (c) 50, (d) 80 and (e) 100. (f) Distribution of the first two PCA components in comparison. This panel shows the same plot as in Fig. 4b.

Chen, H. H.-H., Pineda, J. E., Goodman, A. A., et al. 2019a, *ApJ*, 877, 93, doi: [10.3847/1538-4357/ab1a40](https://doi.org/10.3847/1538-4357/ab1a40)

Chen, H. H.-H., Pineda, J. E., Offner, S. S. R., et al. 2019b, *ApJ*, 886, 119, doi: [10.3847/1538-4357/ab4ce9](https://doi.org/10.3847/1538-4357/ab4ce9)

Chen, M. C.-Y., Di Francesco, J., Rosolowsky, E., et al. 2020, arXiv e-prints, arXiv:2002.11736. <https://arxiv.org/abs/2002.11736>

Dib, S., Hennebelle, P., Pineda, J. E., et al. 2010, *ApJ*, 723, 425, doi: [10.1088/0004-637X/723/1/425](https://doi.org/10.1088/0004-637X/723/1/425)

Draine, B. T. 2003, *ARA&A*, 41, 241, doi: [10.1146/annurev.astro.41.011802.094840](https://doi.org/10.1146/annurev.astro.41.011802.094840)

Dullemond, C. P., Juhasz, A., Pohl, A., et al. 2012, RADMC-3D: A multi-purpose radiative transfer tool, Astrophysics Source Code Library. <http://ascl.net/1202.015>

Ebert, R. 1955, *ZA*, 37, 217

Enoch, M. L., Evans, II, N. J., Sargent, A. I., et al. 2008, *ApJ*, 684, 1240, doi: [10.1086/589963](https://doi.org/10.1086/589963)

Friesen, R. K., Pineda, J. E., co-PIs, et al. 2017, *ApJ*, 843, 63, doi: [10.3847/1538-4357/aa6d58](https://doi.org/10.3847/1538-4357/aa6d58)

Fuller, G. A., & Myers, P. C. 1992, *ApJ*, 384, 523, doi: [10.1086/170894](https://doi.org/10.1086/170894)

Ginsburg, A., & Mirocha, J. 2011, PySpecKit: Python Spectroscopic Toolkit, Astrophysics Source Code Library. <http://ascl.net/1109.001>

Goldsmith, P. F. 2001, *ApJ*, 557, 736, doi: [10.1086/322255](https://doi.org/10.1086/322255)

Goodman, A. A., Barranco, J. A., Wilner, D. J., & Heyer, M. H. 1998, *ApJ*, 504, 223, doi: [10.1086/306045](https://doi.org/10.1086/306045)

Goodman, A. A., Benson, P. J., Fuller, G. A., & Myers, P. C. 1993, *ApJ*, 406, 528, doi: [10.1086/172465](https://doi.org/10.1086/172465)

Goodman, A. A., Pineda, J. E., & Schnee, S. L. 2009a, *ApJ*, 692, 91, doi: [10.1088/0004-637X/692/1/91](https://doi.org/10.1088/0004-637X/692/1/91)

Goodman, A. A., Rosolowsky, E. W., Borkin, M. A., et al. 2009b, *Nature*, 457, 63, doi: [10.1038/nature07609](https://doi.org/10.1038/nature07609)

Guszejnov, D., & Hopkins, P. F. 2015, *MNRAS*, 450, 4137, doi: [10.1093/mnras/stv872](https://doi.org/10.1093/mnras/stv872)

Hacar, A., & Tafalla, M. 2011, *A&A*, 533, A34, doi: [10.1051/0004-6361/201117039](https://doi.org/10.1051/0004-6361/201117039)

Hacar, A., Tafalla, M., Kauffmann, J., & Kovács, A. 2013, *A&A*, 554, A55, doi: [10.1051/0004-6361/201220090](https://doi.org/10.1051/0004-6361/201220090)

Hennebelle, P., & Chabrier, G. 2008, *ApJ*, 684, 395, doi: [10.1086/589916](https://doi.org/10.1086/589916)

—. 2009, *ApJ*, 702, 1428, doi: [10.1088/0004-637X/702/2/1428](https://doi.org/10.1088/0004-637X/702/2/1428)

Hennebelle, P., & Falgarone, E. 2012, *A&A Rv*, 20, 55, doi: [10.1007/s00159-012-0055-y](https://doi.org/10.1007/s00159-012-0055-y)

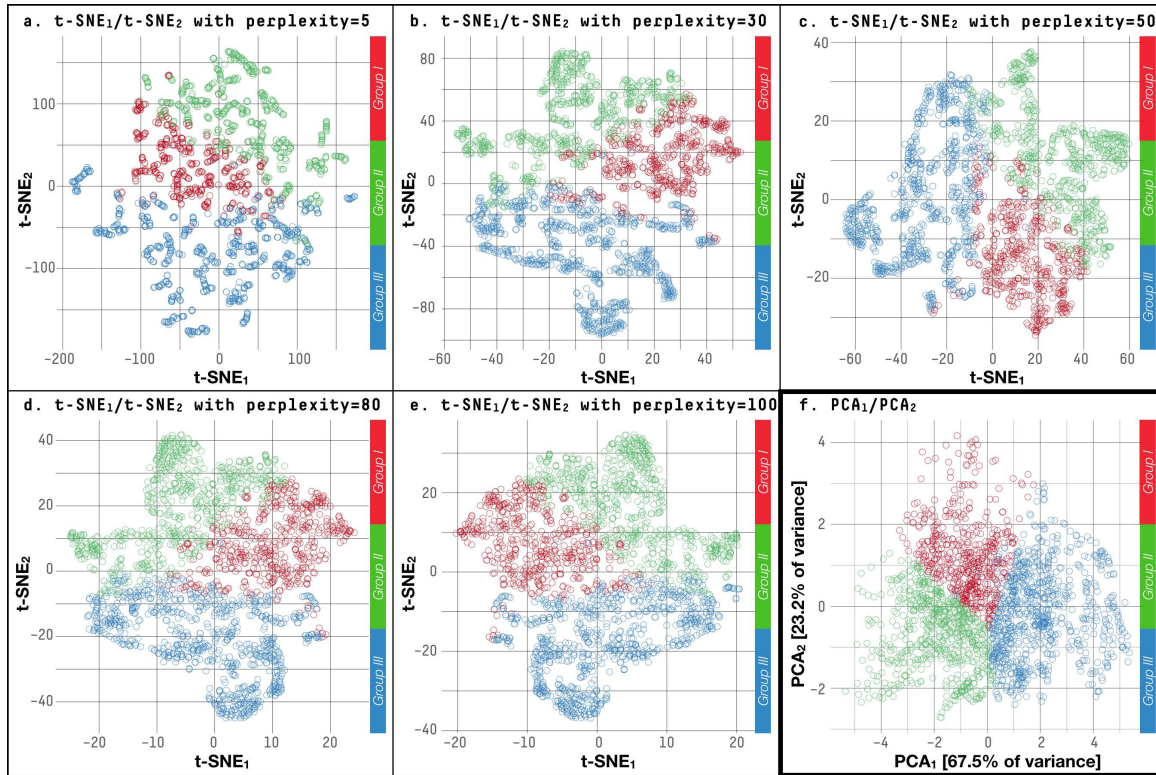


**Figure 19.** Same as Fig. 17, but the data points are color coded by the core phases derived in §3.3. The t-SNE distributions are derived with perplexity of (a) 5, (b) 30, (c) 50, (d) 80 and (e) 100. (f) Distribution of the first two PCA components in comparison. This panel shows the same plot as in Fig. 5.

Henshaw, J. D., Caselli, P., Fontani, F., et al. 2016, MNRAS, 463, 146, doi: [10.1093/mnras/stw1794](https://doi.org/10.1093/mnras/stw1794)

Hopkins, P. F. 2013, MNRAS, 430, 1653, doi: [10.1093/mnras/sts704](https://doi.org/10.1093/mnras/sts704)

Jijina, J., Myers, P. C., & Adams, F. C. 1999, ApJS, 125, 161, doi: [10.1086/313268](https://doi.org/10.1086/313268)

Kainulainen, J., Stutz, A. M., Stanke, T., et al. 2017, A&A, 600, A141, doi: [10.1051/0004-6361/201628481](https://doi.org/10.1051/0004-6361/201628481)

Kauffmann, J., Bertoldi, F., Bourke, T. L., Evans, II, N. J., & Lee, C. W. 2008, A&A, 487, 993, doi: [10.1051/0004-6361:200809481](https://doi.org/10.1051/0004-6361:200809481)

Kirk, H., Pineda, J. E., Johnstone, D., & Goodman, A. 2010, ApJ, 723, 457, doi: [10.1088/0004-637X/723/1/457](https://doi.org/10.1088/0004-637X/723/1/457)

Klessen, R. S. 2001, ApJ, 556, 837, doi: [10.1086/321626](https://doi.org/10.1086/321626)

Klessen, R. S., Ballesteros-Paredes, J., Vázquez-Semadeni, E., & Durán-Rojas, C. 2005, ApJ, 620, 786, doi: [10.1086/427255](https://doi.org/10.1086/427255)

Koch, E. W., Ward, C. G., Offner, S., Loeppky, J. L., & Rosolowsky, E. W. 2017, MNRAS, 471, 1506, doi: [10.1093/mnras/stx1671](https://doi.org/10.1093/mnras/stx1671)

Krumholz, M. R., Klein, R. I., McKee, C. F., & Bolstad, J. 2007, ApJ, 667, 626, doi: [10.1086/520791](https://doi.org/10.1086/520791)

Krumholz, M. R., McKee, C. F., & Klein, R. I. 2004, ApJ, 611, 399, doi: [10.1086/421935](https://doi.org/10.1086/421935)

Lada, C. J., Bergin, E. A., Alves, J. F., & Huard, T. L. 2003, ApJ, 586, 286, doi: [10.1086/367610](https://doi.org/10.1086/367610)

Lada, C. J., Muench, A. A., Rathborne, J., Alves, J. F., & Lombardi, M. 2008, ApJ, 672, 410, doi: [10.1086/523837](https://doi.org/10.1086/523837)

Li, P. S., Martin, D. F., Klein, R. I., & McKee, C. F. 2012, ApJ, 745, 139, doi: [10.1088/0004-637X/745/2/139](https://doi.org/10.1088/0004-637X/745/2/139)

Li, P. S., Norman, M. L., Mac Low, M.-M., & Heitsch, F. 2004, ApJ, 605, 800, doi: [10.1086/382652](https://doi.org/10.1086/382652)

Lu, X., Zhang, Q., Liu, H. B., et al. 2018, ApJ, 855, 9, doi: [10.3847/1538-4357/aaad11](https://doi.org/10.3847/1538-4357/aaad11)

Mairs, S., Johnstone, D., Offner, S. S. R., & Schnee, S. 2014, ApJ, 783, 60, doi: [10.1088/0004-637X/783/1/60](https://doi.org/10.1088/0004-637X/783/1/60)

McKee, C. F., & Ostriker, E. C. 2007, ARA&A, 45, 565, doi: [10.1146/annurev.astro.45.051806.110602](https://doi.org/10.1146/annurev.astro.45.051806.110602)

McKee, C. F., & Tan, J. C. 2002, Nature, 416, 59, doi: [10.1038/416059a](https://doi.org/10.1038/416059a)

—. 2003, ApJ, 585, 850, doi: [10.1086/346149](https://doi.org/10.1086/346149)

Myers, P. C. 2009, ApJ, 700, 1609, doi: [10.1088/0004-637X/700/2/1609](https://doi.org/10.1088/0004-637X/700/2/1609)

Myers, P. C., Fuller, G. A., Goodman, A. A., & Benson, P. J. 1991, ApJ, 376, 561, doi: [10.1086/170305](https://doi.org/10.1086/170305)

Myers, P. C., Linke, R. A., & Benson, P. J. 1983, ApJ, 264, 517, doi: [10.1086/160619](https://doi.org/10.1086/160619)

- Offner, S. S. R., & Arce, H. G. 2015, *ApJ*, 811, 146, doi: [10.1088/0004-637X/811/2/146](https://doi.org/10.1088/0004-637X/811/2/146)
- Offner, S. S. R., Klein, R. I., & McKee, C. F. 2008, *ApJ*, 686, 1174, doi: [10.1086/590238](https://doi.org/10.1086/590238)
- Ortiz-León, G. N., Loinard, L., Kounkel, M. A., et al. 2017, *ApJ*, 834, 141, doi: [10.3847/1538-4357/834/2/141](https://doi.org/10.3847/1538-4357/834/2/141)
- Padoan, P., & Nordlund, Å. 2002, *ApJ*, 576, 870, doi: [10.1086/341790](https://doi.org/10.1086/341790)
- Padoan, P., Nordlund, A., & Jones, B. J. T. 1997, *MNRAS*, 288, 145, doi: [10.1093/mnras/288.1.145](https://doi.org/10.1093/mnras/288.1.145)
- Padoan, P., Pan, L., Juvela, M., Haugbølle, T., & Nordlund, Å. 2019, arXiv e-prints, arXiv:1911.04465. <https://arxiv.org/abs/1911.04465>
- Palau, A., Ballesteros-Paredes, J., Vázquez-Semadeni, E., et al. 2015, *MNRAS*, 453, 3785, doi: [10.1093/mnras/stv1834](https://doi.org/10.1093/mnras/stv1834)
- Pattle, K., Ward-Thompson, D., Kirk, J. M., et al. 2015, *MNRAS*, 450, 1094, doi: [10.1093/mnras/stv376](https://doi.org/10.1093/mnras/stv376)
- Pineda, J. E., Goodman, A. A., Arce, H. G., et al. 2010, *ApJL*, 712, L116, doi: [10.1088/2041-8205/712/1/L116](https://doi.org/10.1088/2041-8205/712/1/L116)
- Pineda, J. E., Offner, S. S. R., Parker, R. J., et al. 2015, *Nature*, 518, 213, doi: [10.1038/nature14166](https://doi.org/10.1038/nature14166)
- Ragan, S. E., Henning, T., Beuther, H., Linz, H., & Zahorecz, S. 2015, *A&A*, 573, A119, doi: [10.1051/0004-6361/201424948](https://doi.org/10.1051/0004-6361/201424948)
- Ridge, N. A., Di Francesco, J., Kirk, H., et al. 2006, *AJ*, 131, 2921, doi: [10.1086/503704](https://doi.org/10.1086/503704)
- Robitaille, T., Beaumont, C., Qian, P., Borkin, M., & Goodman, A. 2017, glueviz v0.13.1: multidimensional data exploration glueviz v0.13.1: multidimensional data exploration, doi: [10.5281/zenodo.1237692](https://doi.org/10.5281/zenodo.1237692). <https://doi.org/10.5281/zenodo.1237692>
- Rosolowsky, E. W., Pineda, J. E., Foster, J. B., et al. 2008a, *ApJS*, 175, 509, doi: [10.1086/524299](https://doi.org/10.1086/524299)
- Rosolowsky, E. W., Pineda, J. E., Kauffmann, J., & Goodman, A. A. 2008b, *ApJ*, 679, 1338, doi: [10.1086/587685](https://doi.org/10.1086/587685)
- Seo, Y. M., Shirley, Y. L., Goldsmith, P., et al. 2015, *ApJ*, 805, 185, doi: [10.1088/0004-637X/805/2/185](https://doi.org/10.1088/0004-637X/805/2/185)
- Seo, Y. M., Majumdar, L., Goldsmith, P. F., et al. 2019, *ApJ*, 871, 134, doi: [10.3847/1538-4357/aaf887](https://doi.org/10.3847/1538-4357/aaf887)
- Shu, F. H. 1977, *ApJ*, 214, 488, doi: [10.1086/155274](https://doi.org/10.1086/155274)
- Shu, F. H., Adams, F. C., & Lizano, S. 1987, *Annual Review of Astronomy and Astrophysics*, 25, 23, doi: [10.1146/annurev.aa.25.090187.000323](https://doi.org/10.1146/annurev.aa.25.090187.000323)
- Smith, R. J., Glover, S. C. O., Klessen, R. S., & Fuller, G. A. 2016, *MNRAS*, 455, 3640, doi: [10.1093/mnras/stv2559](https://doi.org/10.1093/mnras/stv2559)
- Smith, R. J., Longmore, S., & Bonnell, I. 2009, *MNRAS*, 400, 1775, doi: [10.1111/j.1365-2966.2009.15621.x](https://doi.org/10.1111/j.1365-2966.2009.15621.x)
- Smith, R. J., Shetty, R., Stutz, A. M., & Klessen, R. S. 2012, *ApJ*, 750, 64, doi: [10.1088/0004-637X/750/1/64](https://doi.org/10.1088/0004-637X/750/1/64)
- Smullen, R. A., Kratter, K. M., Offner, S. S. R., Lee, A. T., & Chen, H. H.-H. 2020, arXiv e-prints, arXiv:2004.01263. <https://arxiv.org/abs/2004.01263>
- Suri, S., Sánchez-Monge, Á., Schilke, P., et al. 2019, *A&A*, 623, A142, doi: [10.1051/0004-6361/201834049](https://doi.org/10.1051/0004-6361/201834049)
- Suzuki, H., Yamamoto, S., Ohishi, M., et al. 1992, *ApJ*, 392, 551, doi: [10.1086/171456](https://doi.org/10.1086/171456)
- Tafalla, M., & Hacar, A. 2015, *A&A*, 574, A104, doi: [10.1051/0004-6361/201424576](https://doi.org/10.1051/0004-6361/201424576)
- Tafalla, M., Myers, P. C., Caselli, P., & Walmsley, C. M. 2004, *A&A*, 416, 191, doi: [10.1051/0004-6361:20031704](https://doi.org/10.1051/0004-6361:20031704)
- Tan, J. C., Beltrán, M. T., Caselli, P., et al. 2014, in *Protostars and Planets VI*, ed. H. Beuther, R. S. Klessen, C. P. Dullemond, & T. Henning, 149
- Tan, J. C., Kong, S., Butler, M. J., Caselli, P., & Fontani, F. 2013, *ApJ*, 779, 96, doi: [10.1088/0004-637X/779/2/96](https://doi.org/10.1088/0004-637X/779/2/96)
- The Astropy Collaboration, Price-Whelan, A. M., Sipőcz, B. M., et al. 2018, ArXiv e-prints. <https://arxiv.org/abs/1801.02634>
- Traven, G., Matijević, G., Zwitter, T., et al. 2017, *ApJS*, 228, 24, doi: [10.3847/1538-4365/228/2/24](https://doi.org/10.3847/1538-4365/228/2/24)
- van der Maaten, L., & Hinton, G. 2008, *Journal of Machine Learning Research*, 9, 2579
- Vázquez-Semadeni, E., Gómez, G. C., Jappsen, A. K., Ballesteros-Paredes, J., & Klessen, R. S. 2009, *ApJ*, 707, 1023, doi: [10.1088/0004-637X/707/2/1023](https://doi.org/10.1088/0004-637X/707/2/1023)
- Vázquez-Semadeni, E., González-Samaniego, A., & Colín, P. 2017, *MNRAS*, 467, 1313, doi: [10.1093/mnras/stw3229](https://doi.org/10.1093/mnras/stw3229)
- Ward-Thompson, D., Nutter, D., Bontemps, S., Whitworth, A., & Attwood, R. 2006, *MNRAS*, 369, 1201, doi: [10.1111/j.1365-2966.2006.10356.x](https://doi.org/10.1111/j.1365-2966.2006.10356.x)
- Zinnecker, H. 1982, *Annals of the New York Academy of Sciences*, 395, 226, doi: [10.1111/j.1749-6632.1982.tb43399.x](https://doi.org/10.1111/j.1749-6632.1982.tb43399.x)
- Zucker, C., Speagle, J. S., Schlafly, E. F., et al. 2019, arXiv e-prints, arXiv:1902.01425. <https://arxiv.org/abs/1902.01425>